Oscillation effects and time variation of the supernova neutrino signal

James P. Kneller*
School of Physics and Astronomy, University of Minnesota, Minneapolis, Minnesota 55455, USA

Gail C. McLaughlin† and Justin Brockman‡,§
Department of Physics, North Carolina State University, Raleigh, North Carolina 27695-8202, USA
(Received 15 June 2007; revised manuscript received 18 December 2007; published 19 February 2008)

The neutrinos detected from the next galactic core-collapse supernova will contain valuable information on the internal dynamics of the explosion. One mechanism leading to a temporal evolution of the neutrino signal is the variation of the induced neutrino flavor mixing driven by changes in the density profile. With one and two-dimensional hydrodynamical simulations we identify the behavior and properties of prominent features of the explosion. Using these results we demonstrate the time variation of the neutrino crossing probabilities due to changes in the Mikheyev-Smirnov-Wolfenstein (MSW) neutrino transformations as the star explodes by using the *S*-matrix—Monte Carlo—approach to neutrino propagation. After adopting spectra for the neutrinos emitted from the proto-neutron star we calculate for a galactic supernova the evolution of the positron spectra within a water Cerenkov detector and find that this signal allows us to probe of a number of explosion features.

DOI: 10.1103/PhysRevD.77.045023 PACS numbers: 14.60.Pq, 97.60.Bw

I. INTRODUCTION

The importance of neutrinos in the explosions of massive stars has long been recognized. This significance is coupled with their ability to carry information to us about the processes and conditions in the core of the supernova (SN) so that the neutrino signal from the next galactic supernova will provide us with an opportunity to test the core-collapse paradigm. The explosion begins when the runaway process of electron capture in the core of a massive star leads to a rapid compression and collapse that is only halted when the degenerate pressure of the neutrons and thermal pressure of nondegenerate particles kicks in at supernuclear densities. The rapid neutronization during the collapse leads to a large burst of ν_e neutrinos that identifies the beginning of the event. As nuclear densities are reached the mean free path of the neutrinos becomes shorter than the size of the proto-neutron star and the neutrinos become trapped. Thermal processes within the core create a thermal bath of neutrino-antineutrino pairs of all flavors. The neutrinos slowly diffuse from the core over a period of order 10 seconds, carrying 99% of the gravitational binding energy of the core with them. With such a large neutrino luminosity even a small number of neutrino interactions above the core can create an important impact on the explosion physics. Indeed for collapsing stars with degenerate CO or ONeMg cores neutrino heating can lead to an explosion [1–3]. Detection of the neutrinos from the next nearby supernova will offer us the opportunity to examine the internal evolution of the explosion since the neutrinos allow us to see down all the way to the proto-neutron star. For example, if the proto-neutron star collapses to a black hole, the resulting neutrino signal will be altered [4,5].

In addition, although the neutrinos are only weakly interacting they can have significant effects upon the nucleosynthesis that occurs in the supernova: in the outer layers of the star neutrinos can cause a transformation of the elements synthesized during the preceding thermonuclear burning period in the ''neutrino process'' [6,7], it is thought that a neutrino driven wind occurs at late time in the supernova which may create sufficiently neutron rich material to produce the *r*-process elements [8], and long duration gamma ray bursts (which are thought to be a rare type of supernova) produce elements in conditions governed by strong neutrino fluxes [9,10]. The results of all these nucleosynthesis processes are quite sensitive to the neutrino spectra [11–14].

For reasons pertaining to both hydrodynamics and to element synthesis it is important to understand the details of neutrino propagation in the supernova and the mixing between neutrino flavors. Neutrino oscillations also alter what we observe but, simultaneously, also allow the possibility of elucidating yet unknown neutrino oscillation physics, e.g. [15–19]. Supernova neutrino flavor transformation is a rapidly developing field with the neutrino background terms the subject of intense study [20–26]. Realistic possibilities include a complete mixing of all flavors [20] or a partial oscillation between flavors [23]. An important part of any future observation of supernova neutrinos will be to understand this physics. In parallel, phase effects due to multiple resonances have recently been recognized [27,28] distorting the simple picture of neutrino propagation through the outer layers of the super-

*kneller@physics.umn.edu
†Gail_McLaughlin@ncsu.edu
‡Current address: Department of Applied Physics, Stanford University, Stanford, CA 94305-4090, USA.
§Justin_Brockman@ncsu.edu

nova that have been used in the past [15–17]. The explosion of the star leads to an evolution of the flavor mixing so that to appreciate the effects upon neutrino propagation it is important to understand the density profile.

Observations of high pulsar velocities and polarized supernova light suggest an inherent asymmetry in the explosion mechanism. Though many possible mechanisms for generating the asymmetry have been proposed, recent work by Blondin, Mezzacappa, and DeMarino [29] has identified an instability of the standing accretion shock that leads to large dipole and quadrupole moments. More recent work by Blondin and Mezzacappa [30] and Ohnishi, Kotake, and Yamada [31] as well as Scheck *et al.* [32] has both confirmed and furthered the understanding of this instability. An alternative mechanism, acoustic heating, has also been discussed by Burrows *et al.* [33]. The temporal evolution of the neutrino flavor mixing and the subsequent variation of the neutrino signal means that it may be possible to detect prominent features of the supernova density profile and to use this information to learn important information about the explosion. This possibility was demonstrated first by Schirato and Fuller [34] who used a time-dependent, one-dimensional $1/r^{2.4}$ density profile to demonstrate that the supernova's forward shock wave reaches and disrupts the "H" resonance transformation layer a few seconds after the core bounce leading to a detectable change in the charged-current neutrino signal. This was followed and elaborated upon by Dighe and Smirnov [16], Takahashi *et al.* [35], and Fogli *et al.* [36]. More recently Tomàs *et al.* [37] used a more sophisticated numerical model of a progenitor star to investigate the effect of both forward and reverse shocks on the neutrino signal. Tomàs *et al.* also present one second of a two-dimensional simulation result to show how the density profile can be greatly complicated by a deformed forward shock followed by strong convection currents. But due to the intensive computational burden of supernova models it is numerically very taxing to watch these explosions propagate outward until they affect neutrino transformations.

In this paper we present calculations which link hydrodynamical simulations of time-dependent density profiles and phase-retaining neutrino oscillations. Our presentation begins in Sec. II with the results from simulations of supernovae in both one and two dimensions where we artificially heat a density profile constructed so as to mimic the state of the supernova at the point where the accretion shock has stalled. Our two-dimensional explosions are heated aspherically so as to create an aspherical supernova. Though this 2D model lacks some structural features present in more sophisticated models that generate asphericity via standing accretion shock instabilities, we still obtain results that give a good idea of how density anisotropy affects neutrino flavor transformations. In Sec. III we pass a spectrum of neutrinos through the simulation results and show how the crossing probability is affected by the evolution of the profiles. We finish in Sec. IV by presenting our calculation of the positron spectra within a water Cerenkov detector to demonstrate our ability to extract information about the supernova.

II. THE SN PROFILE

A. The SN simulations

Our first task in determining the neutrino signal is to simulate the supernova so as to obtain the time evolution of the density profile. A supernova simulation is a complex and computationally intensive problem. At the present time there is not yet a robust, self-consistent model for core-collapse supernovae, and the most sophisticated multidimensional simulations take a very long time to compute. But we do not need to simulate the actual core collapse and formation of the proto-neutron star; these events occur deep within the core at a radius of 10^7 cm or so, whereas the first neutrino resonance occurs at around 10^9 cm for neutrino energies of order 10 MeV, and the second is even further out. What is occurring in the core is irrelevant for our purposes. All we need from the simulation of the supernova is the propagation of the shock through the star. For this reason we employ a simplistic and artificially energetic numerical simulation to create explosions with a range of features that might be present in reality. We do not intend this model to be realistic itself, but rather a tool to help with the difficult problem of reconstructing density features of an exploding star based on changing neutrino signals detected at Earth.

We use VH-1 [38], a hydrodynamic code based on Woodward and Colella's [39] piecewise parabolic method. For both the one-dimensional and two-dimensional simulations we employ an exponentially coarsening radial grid that ranges from $r = 10$ km to $r = 250\,000$ km where r is the radius from the center of the star, and for the two-dimensional simulations an angular grid that ranges from $\theta = 0$ to $\theta = \pi$ where θ is the polar angle. The innermost radial grid increment is set to $\delta r = 202.6$ m and increases by 1.3% thereafter. By $r = 10^3$ km the radial increment has grown to $\delta r \sim 6.5$ km and by $r = 10^5$ km we reach $\delta r \sim 650$ km. We map into the code a spherically symmetric progenitor profile intended to represent the state of the supernova about 100 ms after the collapse. Beyond $r = 200$ km the profile is that of a low metallicity, $13.2M_\odot$ progenitor model developed by Heger *et al.* [40] that we have allowed to collapse further within VH-1 so that the infall velocities approached free fall. Interior to $r = 200$ km we splice in a slow, outward-moving standing accretion shock profile provided by Heywood [41] that is similar to that found in [29]. Finally, inside $r = 20$ km we insert a dense, $\gamma = 2.5$, polytropic core containing approximately $3M_\odot$. The inner boundary condition inside the dense core at 10 km is reflecting. Figure 1 shows the full initial density profile. To drive the explosion, we mimic neutrino heating by inserting energy into the region above

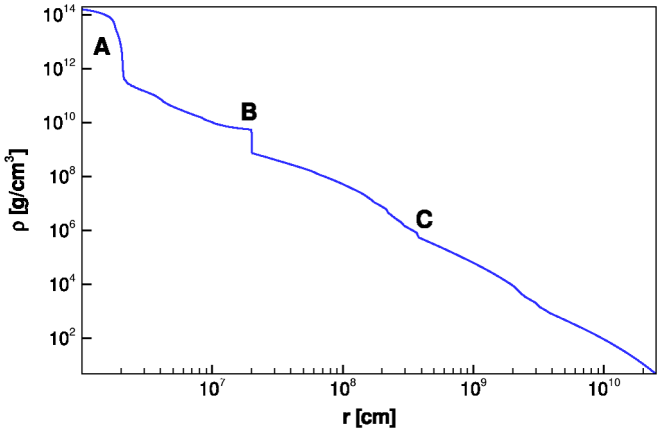

FIG. 1 (color online). The initial, $t = 0$, density profile used in our SN simulations. The dense core (A) inside 20 km contains approximately $3M_\odot$. The slow, outward-moving standing accretion shock (B) is located at 200 km. Above that we have a collapsing, $13.2M_\odot$, progenitor (C).

a $r_g = 100$ km gain radius. The energy deposition rate per unit volume, $dQ/dtdV$, is proportional to the density of material, falls as $1/r^2$, and decreases exponentially with time t over a time scale τ set to $\tau = 0.5$ s. For the 1D simulations then,

$$\frac{dQ}{dtdV} \propto \frac{\rho}{r^2}\left(\frac{r - r_g}{r}\right)te^{-t/\tau}. \quad (1)$$

The additional factors of $(r - r_g)/r$ and t are inserted so as to ramp up the energy deposition over both distance and time thereby avoiding the violent disruption that occurs if we deposit energy either too suddenly or within a small volume. For the 2D models we introduce an angular dependence into the energy deposition prescription so as to match the observation by Blondin *et al.* [29] that small perturbations in standing accretion shock models can ultimately lead to aspherical shock modes. We break the spherical symmetry of our 2D simulations by heating the initial profile with a combination of 80% spherical mode heating and 20% $\sin^2\theta$ mode heating. Thus for the 2D cases $dQ/dtdV$ becomes

$$\frac{dQ}{dtdV} \propto \frac{\rho}{r^2}\left(\frac{r - r_g}{r}\right)te^{-t/\tau}(1 + 0.5\sin^2\theta). \quad (2)$$

In either case the total energy, Q, input during the simulation was recorded. Below the gain radius we wish to maintain the spherical density/gravity conditions and to prevent mass from escaping the core so that we do not disturb the shock heating and convective flow in the outer star. In a real supernova the core is stabilized by neutrino emission but in lieu of full implementation of this cooling mechanism our simulations achieve the same result by forcing all radial and angular velocities below r_g to zero. In this way we separate the evolution of the outer layers of the star from the complex behavior near the core. The runtime of the 1D simulations is sufficiently short that we can vary the total energy deposition thereby obtaining a variety of results ranging from weak explosions through to the very powerful. The 2D simulations take much longer to run and so we have just one data set with an explosion energy set to 3×10^{51} erg.

Before presenting our simulation results we mention that in general, numerical schemes tend to spread the shock front over several zones and they therefore become artificially softened. Schirato and Fuller [34] account for this artifact by steepening by hand the density profile at the shocks. The shocks in our simulations are sufficiently steep to demonstrate the primary effect on neutrino mixing, therefore we do not implement a similar correction.

B. Simulation results

The density profiles of the SN we obtain from the simulations possess noticeable differences as the energy deposition changes. For weak explosions the profiles are monotonically decreasing functions of the radius, r, with a single, forward facing, shock front that moves relatively slowly outwards. As the deposition energy increases a lower-density cavity forms behind the shock. Further increases in Q eventually lead to the formation of a reverse shock behind the lower-density zone. All three features are present in the results of the 2D simulations but the higher dimensionality, coupled with the aspherical heating, means that this SN possesses a much more turbulent/chaotic profile. In Fig. 2 we show a time slice of the 2D SN simulation. The forward shock is seen at "A," the "reverse

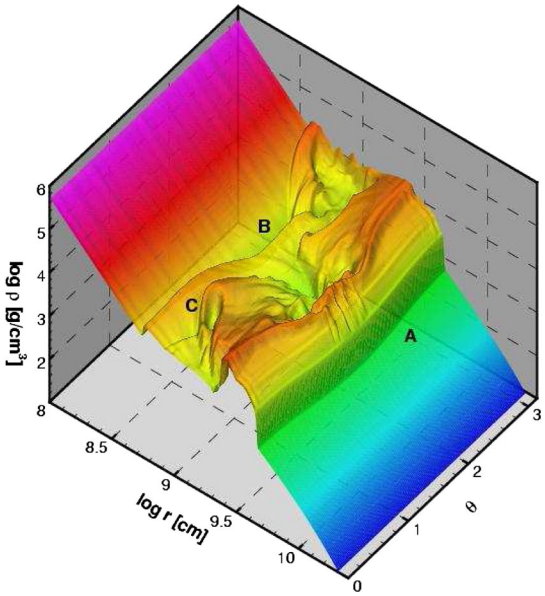

FIG. 2 (color online). The density as a function of the radius and angle in a 2D SN model at $t = 2.5$ s. The forward shock is located to the left of "A," the reverse shock is the step-up in density found to the right of "B," and one of the many local cavities in the profile between the shocks is to the right of "C."

shock'' is at ''B,'' and one of the many bubbles in the density profile is located at ''C.'' We note that although our applied neutrino heating is symmetric about the equator ($\theta = \pi/2$) the resulting density profile is not. We attribute this to the inherent instability of multidimensional accretion shocks, potentially excited by simulation numerics. In what follows we discuss the behavior and properties of the various features of the profile.

1. The forward shock

The forward shock is a generic feature of supernovae simulations. A stalled forward shock was present in the initial profile inserted into the hydrodynamical code and the heating we introduced was meant to revive its outward motion. After revival the shock propagates out through the star and is the explosion feature furthest from the proto-neutron star. The forward shock is visible in Fig. 2 as the large jump in density at larger radii and we note that the forward shock in the 2D simulation is slightly oblate due to the aspherical heating of the material. We study the behavior of the forward shock with various explosion strengths using the 1D simulations.

In Fig. 3 we show four snapshots of the density profile in a one-dimensional simulation in which the total energy deposition was $Q = 1.66 \times 10^{51}$ erg. Actual SN are thought to be more energetic than this so we regard the results from this simulation as being at the lower end of realistic possibilities. This energy is also significantly less than that used in the simulation shown in Fig. 2 and, consequently, the profile is much simpler. The forward shock is clearly visible and we note that the fractional jump in density across it does not vary. For normal shocks the density jump across the shock is given by

$$1 + \frac{\Delta\rho}{\rho} = \frac{(\gamma + 1)M^2}{(\gamma - 1)M^2 + 2}, \tag{3}$$

where M the Mach number and γ is determined by the ratio of specific heats. In our simulations we adopted a fixed equation of state and the Mach number of the shock is always sufficiently large so that we find that the density jump does not vary to any great extent with time and/or with Q. But the position of the forward shock as a function of time is greatly influenced by Q with larger values leading to more rapidly moving forward shocks. This can be seen in Fig. 4 which is snapshots at the same moments as those in Fig. 3 for a 1D simulation with $Q = 3.07 \times 10^{51}$ erg. This figure also displays the low-density cavity that can form behind the forward shock as Q increases. This profile is very similar to the profiles used by Fuller and Schirato [34], Fogli *et al.* [36], and Choubey, Harries, and Ross [42].

2. The reverse shock

The heating that led to the regeneration of the forward shock continues to accelerate the material above the proto-neutron star even after the shock has been revived and is moving outwards. A wind is created with a velocity that increases with radius. When the velocity of the material becomes larger than the local sound speed a reverse shock is formed. The influence of the reverse shock upon the conditions for nucleosynthesis in supernovae has been recently studied by Arcones, Janka, and Scheck [43]. The reverse shock feature was not present in the ''initial'' profile; it develops only later. If a reverse shock is to form enough energy must be deposited to create a sufficiently strong wind. A reverse shock can be seen in Fig. 2 where it is the step-up in density at the back of the turbulent zone behind the forward shock. The reverse shock is oblate due to the aspherical heating of the material in the simulation.

Once again we can use 1D simulations to study this feature more easily. No reverse shock was seen in the

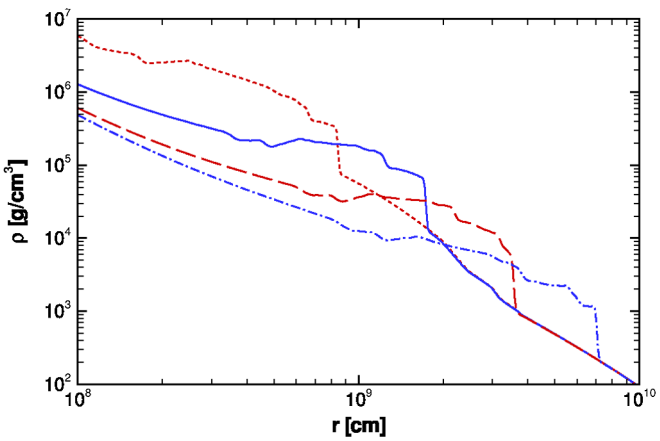

FIG. 3 (color online). The density as a function of the radius in a 1D SN model with $Q = 1.66 \times 10^{51}$ erg at $t = 0.9$ s (dotted line), $t = 1.8$ s (solid line), $t = 3.6$ s (long dashed line), and $t = 7.2$ s (dash-dot line).

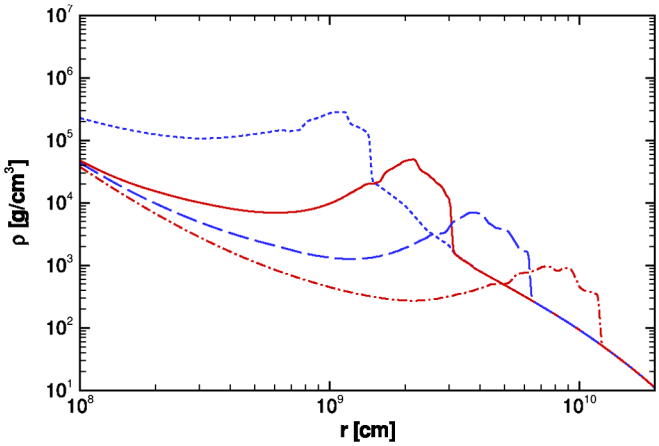

FIG. 4 (color online). The density as a function of the radius in a 1D SN model with $Q = 3.07 \times 10^{51}$ erg at $t = 0.9$ s (dotted line), $t = 1.8$ s (solid line), $t = 3.6$ s (long dashed line), and $t = 7.2$ s (dash-dot line).

profiles shown in Fig. 3 or 4 but when we increase Q to $Q = 3.36 \times 10^{51}$ erg we obtain the results presented in Fig. 5. We notice that the forward shock is, again, moving more rapidly compared to the results shown in Figs. 3 and 4 due to the larger energy deposition Q. The figure also indicates that the reverse shock is smaller than the forward shock. As Q increases further the density jump across the reverse shock increases and it moves closer to the forward shock. We find that it is also possible for the reverse shock to penetrate to densities lower than the forward shock. Both of these behaviors are shown in Fig. 6 where we show snapshots of the profile for a 1D simulation with $Q = 4.51 \times 10^{51}$ erg. The density jump across the reverse shock is still smaller than across the forward but they are almost equivalent, and the density immediately behind the reverse shock is lower than the density immediately in front of the forward shock. It was mentioned by Tomàs *et al.* [37] that this feature was also seen at early times in their simulations. But realistically SN may struggle to achieve explosions with comparable energies so we regard the results of this simulation as being at the upper end of possibilities.

In both Figs. 5 and 6 the reverse shock was driven radially outward by a wind generated by the material heated above the proto-neutron star. Our energy deposition decreased exponentially with time which led to a gradual decrease in wind strength. In turn, as the wind abates, the outward motion of the reverse shock slows and, eventually, we find that its motion can be completely halted. This stalling of the reverse shock also occurred in the two-dimensional simulation with the shock stalling at different times for different polar angles. We also find that in both 1D and 2D simulations the density jump across the reverse shock decreases as the shock is about to turn around. After the reverse shock stalls both the 1D and 2D simulations indicate that the reverse shock feature then moves back towards the core. In Fig. 5 we see this stalling of the reverse shock and the backwards motion can be seen after comparing the profiles at $t = 2.5$ s and $t = 3$ s. The reverse shock in this simulation actually reached its furthest radial position at about $t = 2.4$ s. A similar backwards motion for the reverse shock was seen by both Tomàs *et al.* [37] and Arcones, Janka, and Scheck [43].

Eventually the reverse shock reaches the core whereupon our simulations indicate that it is reflected and subsequently becomes a weak forward shock. Further snapshots of the density profile taken from the simulation with $Q = 3.36 \times 10^{51}$ erg are shown in Fig. 7 where we see more clearly the backwards motion of the reverse shock and its later reflection. The radial position at which the reverse shock stalls depends upon the energy deposition. Additional snapshots from the simulation with slightly larger energy deposition, $Q = 4.51 \times 10^{51}$ erg, are shown in Fig. 8. Though the reverse shock in this

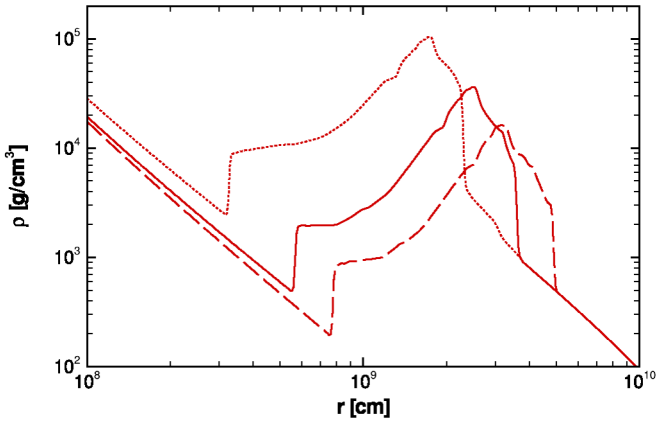

FIG. 6 (color online). The density as a function of the radius in a 1D SN model with $Q = 4.51 \times 10^{51}$ erg at $t = 1.0$ s (dashed line), $t = 1.5$ s (solid line), and $t = 2.0$ s (long dashed line).

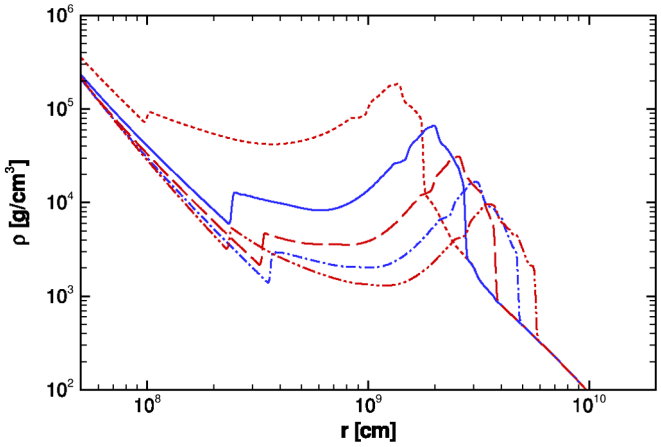

FIG. 5 (color online). The density as a function of the radius in a 1D SN model where $Q = 3.36 \times 10^{51}$ erg at $t = 1$ s (dotted line), $t = 1.5$ s (solid line), $t = 2$ s (long dashed line), $t = 2.5$ s (dash-dot line), and $t = 3$ s (dash double-dot line).

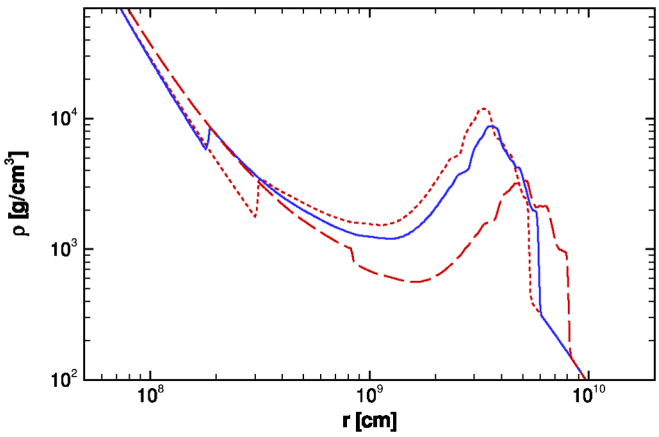

FIG. 7 (color online). The density as a function of the radius in the same 1D SN model shown in Fig. 5, i.e. with $Q = 3.36 \times 10^{51}$ erg, at $t = 2.8$ s (dotted line), $t = 3.3$ s (solid line), and $t = 4.3$ s (long dashed line).

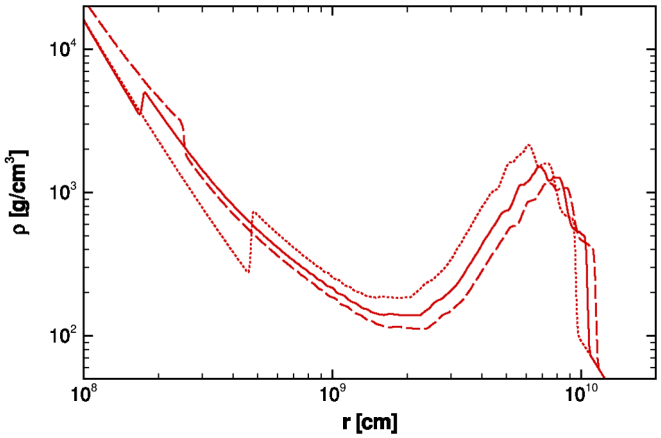

FIG. 8 (color online). The density as a function of the radius in the same 1D SN model shown in Fig. 6, that is $Q = 4.51 \times 10^{51}$ erg, at $t = 4.0$ s (dotted line), $t = 4.5$ s (solid line), and $t = 4.9$ s (long dashed line).

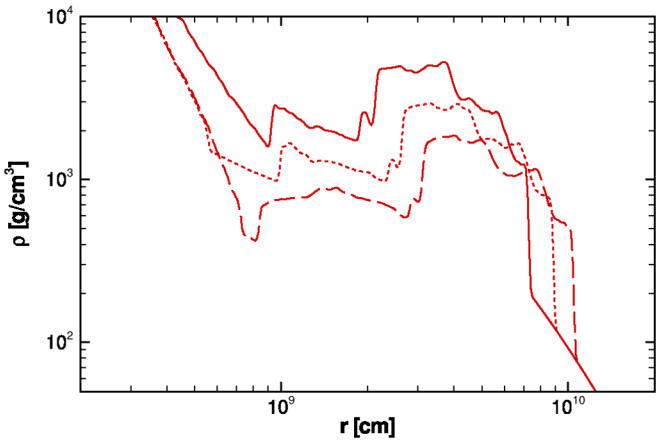

FIG. 9 (color online). The density at a polar angle of 25° as a function of the radius in a 2D SN model at $t = 3.9$ s (solid line), $t = 4.8$ s (dotted line), and $t = 5.7$ s (dashed line).

simulation also attained its maximum radial position at $t = 2.4$ s the figure shows that it was located further out before it was turned around.

The reverse shock is an interesting feature of the SN and, in contrast with the forward shock, can move both outwards and inwards. For a very energetic explosion it may penetrate to lower densities than that immediately in front of the forward shock. The density jump across the reverse shock can vary with time and does so most noticeably when the shock is about to stall.

3. Asphericity

The difference in the hydrodynamics between the one and two-dimensional SN simulations can be traced back to the aspherical heating of the material above the proto-neutron star in the two-dimensional case. Nonspherical heating can lead to turbulent fluid flow creating eddies and bubbles as shown in Fig. 2. The neutrinos released by the proto-neutron star propagate along radial slices of the profile. In Fig. 9 we show the density profile from the 2D model at the polar angle of $\theta = 25°$ for snapshots at $t = 3.9$ s, $t = 4.8$ s, and $t = 5.7$ s while in Fig. 10 we present the density along three different polar angles at $t = 2.5$ s, i.e. taken from Fig. 2. In both we see the forward and reverse shocks and, as mentioned earlier, Fig. 10 also shows that the radial position of both the forward and reverse shocks varies with the polar angle. Figure 9 also indicates that between $t = 4.8$ s and $t = 5.7$ s the reverse shock (along this radial slice) stalled and began to move back to the core. For other radial slices the reverse shock turnaround time will be different: in Fig. 11 we plot radial slices along the 125° line of sight at various times. The reverse shock in the figure, located just beyond $r = 10^9$ cm, turns around between 5.4 s and 6.3 s.

In all our 2D figures the general shape of the density profile between the two shocks is reminiscent of that shown in Fig. 5 for the 1D simulation with a similar value for Q—i.e. a lower-density region in front of the reverse shock, a wall of higher density material behind the forward shock—but clearly there are large "fluctuations" upon this basic trend both between the shocks and behind the reverse shock.

C. Summary

The forward shock, the reverse shocks, contact discontinuities, and the local bubbles/cavities are the features in the density profile with the greatest potential to alter the state of any neutrinos propagating through the SN since they represent the locations within the SN where the density gradient is largest. Large density gradients lead to non-adiabatic evolution of the neutrinos and significant differences compared to the neutrino propagation through the undisturbed profile.

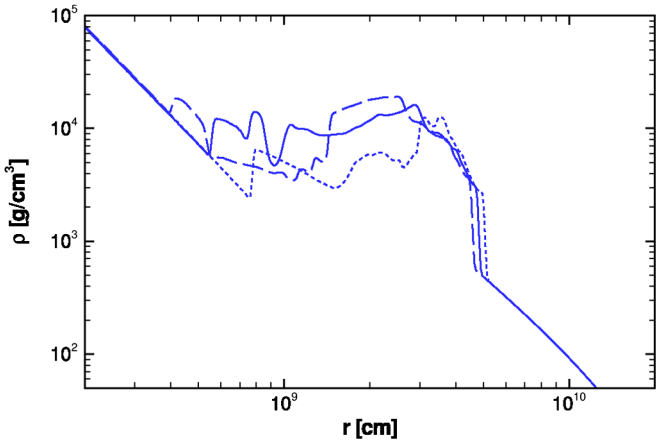

FIG. 10 (color online). The density as a function of the radius in a 2D SN model at $t = 2.5$ s. The angular slices are at 45° (solid line), 105° (dotted line), and 165° (dash-dot line).

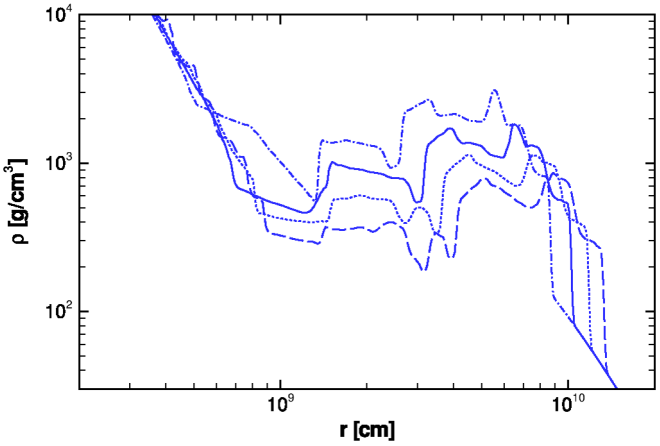

FIG. 11 (color online). The density at a polar angle of 125° as a function of the radius in a 2D SN model at $t = 4.5$ s (dash-dot line), $t = 5.4$ s (solid line), $t = 6.3$ s (dotted line), and $t = 7.2$ s (dashed line).

III. NEUTRINO MIXING

The vast majority of the neutrinos emitted by the supernova last interact with matter at the neutrinosphere located at the surface of the proto-neutron star. As they propagate outwards a small percentage will be absorbed by nucleons thereby transferring energy to the supernova and, it is thought, reviving the stalled shock. But even though the remainder of the neutrinos survive the passage through the material overlying the proto-neutron star what emerges is not the same as what was emitted. The change in the neutrinos is due to neutrino oscillations and the presence of matter modulates this mixing.

Neutrino oscillations arise due to a distinction between the interaction eigenstates (otherwise known as the flavor eigenstates e, μ, τ) and the eigenstates of the free Hamiltonian (known as the mass eigenstates) with masses m_1, m_2, m_3. Since there are three basis states a general neutrino wave function is described by three complex coefficients and evolves according to the Schrödinger equation. In the vacuum the Hamiltonian is diagonal in the mass basis but possesses off-diagonal terms in the flavor basis that are the cause of flavor oscillations. In the presence of matter a potential, $V(\mathbf{r})$, that takes into account coherent forward scattering of the neutrinos, is included in the Hamiltonian. Since we are only concerned with mixing between active neutrino flavors (i.e. all the flavors that have ordinary weak interactions) we may subtract off the common neutral current contribution (which will contribute only an overall phase) leaving just the charged-current contribution to the $\nu_e - \nu_e$ component of $V(\mathbf{r})$. This contribution is the well-known $V_{ee}(\mathbf{r}) = \sqrt{2} G_F Y_e(\mathbf{r}) \rho(\mathbf{r}) / m_N$ where G_F is Fermi's constant, $\rho(\mathbf{r})$ is the mass density, $Y_e(\mathbf{r})$ is the electron fraction, and m_N is the nucleon mass. The effect of the matter upon the antineutrinos differs from that of the neutrinos—the potential $\bar{V}(\mathbf{r})$ that appears in the antineutrino Hamiltonian has the same magnitude but the opposite sign. Because of the inclusion of $V_{ee}(\mathbf{r})$ the Hamiltonian is a function of position and is neither diagonal in the mass basis nor the flavor basis. One may try and diagonalize $H(\mathbf{r})$ but the unitary transformation that relates the flavor basis to the new "matter" basis also varies with the position. Consequently the gradient of the unitary transformation is nonzero and one finds that the Schrodinger equation in this new matter basis—that was meant to diagonalize H—picks up off-diagonal terms. Thus it is not possible, in general, to find a basis that diagonalizes the Hamiltonian and therefore oscillations of the amplitudes that describe the wave function occur in every basis.

In general, the three complex components of the wave function oscillate simultaneously. Exactly what occurs depends upon the energy of the neutrino E, the differences between the squares of the masses m_1, m_2, m_3, the mixing angles that describe the relationship between the flavor and mass basis, and, of course, $V_{ee}(\mathbf{r})$. Since there are three mass eigenstates there are three separate mass splittings $\delta m^2_{ij} = m^2_i - m^2_j$ (though only two are independent) and the relationship between the neutrino flavor and mass bases is described by the matrix U which, in turn, is parametrized by three mixing angles θ_{12}, θ_{13}, and θ_{23} plus a CP-phase δ. The structure of U is

$$U = \begin{pmatrix} c_{12}c_{13} & s_{12}c_{13} & s_{13}e^{-\iota\delta} \\ -s_{12}c_{23} - c_{12}s_{13}s_{23}e^{\iota\delta} & c_{12}c_{23} - s_{12}s_{13}s_{23}e^{\iota\delta} & c_{13}s_{23} \\ s_{12}s_{23} - c_{12}s_{13}c_{23}e^{\iota\delta} & -c_{12}s_{23} - s_{12}s_{13}c_{23}e^{\iota\delta} & c_{13}c_{23} \end{pmatrix}, \quad (4)$$

where $c_{ij} = \cos\theta_{ij}$, $s_{ij} = \sin\theta_{ij}$. Mixing has been observed in the neutrinos emitted by the Sun and the neutrinos produced by cosmic rays striking the atmosphere. Both have been confirmed with terrestrial experiments. Each observation of neutrino mixing can be described by a single $\delta m^2 - \theta$ pair of parameters and experimentally the "solar" and "atmospheric" mass splittings differ by around a factor of $\sim$30 with the solar mass splitting, $\delta m^2_\odot$, being the smaller of the two. This observation permits us to consider the evolution of the general, three component, neutrino wave function as being factored into spatially distinct, two-neutrino mixes. The factorization simplifies matters greatly and from it one can demonstrate that there are two resonances in the supernova density profile: the so-called "L" resonance and the "H" resonance. The L resonance, at lower density and thus further from the proto-neutron star, involves mixing between matter states ν_1 and ν_2, the relevant mass splitting is δm^2_{21}—which is

approximately the solar mass splitting $\delta m^2_\odot$—and the mixing angle is θ_{12}—which is approximately the mixing angle determined by the solar neutrino experiments $\theta_\odot$. The relevant mass eigenstates and mass splitting for the H resonance, at higher density and closer to the core, depend upon the sign of δm^2_{32} (or, equivalently, δm^2_{31}) and this is not currently known. If δm^2_{32} is positive (a normal hierarchy) then the H resonance involves mixing between states ν_2 and ν_3 and the mass splitting δm^2_{32}. If δm^2_{32} is negative (an inverted hierarchy) then at the H resonance it is the antineutrinos states $\bar{\nu}_1$ and $\bar{\nu}_3$ that mix and the relevant mass splitting is $\delta m^2_{31} = \delta m^2_{32} + \delta m^2_{21}$. In either case the mixing angle is the unknown, but small, θ_{13}. Quite generally the coherent matter basis wave function, $\psi_\nu(r, E)$, is related to the initial matter basis wave function $\psi_\nu(0, E)$ via the equation $\psi_\nu(r, E) = S_\nu(r, E)\psi_\nu(0, E)$ while for the antimatter states $\psi_{\bar{\nu}}(r, E) = S_{\bar{\nu}}(r, E)\psi_{\bar{\nu}}(0, E)$. The matrices S_ν and $S_{\bar{\nu}}$ are the S-matrices for the neutrinos and antineutrinos, respectively, for a discussion of this approach to neutrino oscillations, see e.g. [27]. To determine $\psi_\nu(r, E)$ and $\psi_{\bar{\nu}}(r, E)$ we need to know both the initial states $\psi_\nu(0, E)$ and $\psi_{\bar{\nu}}(0, E)$ and the two matrices S_ν and $S_{\bar{\nu}}$.

The matrices $S_\nu(E)$ and $S_{\bar{\nu}}(E)$ can be factored as $S_\nu(E) = S_{V,\nu}(E)S_{L,\nu}(E)S_{H,\nu}(E)S_{SI,\nu}(E)$ and $S_{\bar{\nu}}(E) = S_{V,\bar{\nu}}(E)S_{H,\bar{\nu}}(E)S_{SI,\bar{\nu}}(E)$ which are sufficiently general to accommodate our lack of knowledge of the hierarchy. The two matrices $S_{V,\nu}(E)$ and $S_{V,\bar{\nu}}(E)$ represent the neutrino propagation from the surface of the SN through the vacuum to Earth and both are diagonal in the mass basis. The matrices $S_{H,\nu}(E)$, $S_{H,\bar{\nu}}(E)$, and $S_{L,\nu}(E)$ represent the change due to the neutrino's or antineutrino's passage through the H or L resonance.[1] There is no matrix $S_{L,\bar{\nu}}(E)$ because antineutrinos do not experience an L resonance in matter. Finally, neutrino self-interactions—described in Samuel [44], Pastor, Raffelt, and Semikoz [45], and Friedland and Lunardini [19]—in the region immediately above the proto-neutron star can alter the spectra before the H resonance layer. These effects are described by the matrices $S_{SI,\nu}(E)$ and $S_{SI,\bar{\nu}}(E)$. The two matrices $S_{SI,\nu}(E)$ and $S_{SI,\bar{\nu}}(E)$ are evaluated after the self-interactions have ceased but before the H resonances, while $S_{H,\nu}(E)$ and $S_{H,\bar{\nu}}(E)$ are evaluated somewhere between the H and L resonances and $S_L(E)$ is evaluated at the surface of the SN. These evaluation positions will not affect our result if they are sufficiently far from the resonances and the regions where self-interactions occur.

The structures of $S_{H,\nu}(E)$, $S_{H,\bar{\nu}}(E)$, and $S_{L,\nu}(E)$ follow from our knowledge of the matter states that mix at the H or L resonances. This structure is

$$S_{L,\nu}(E) = \begin{pmatrix} \alpha_L(E) & \beta_L(E) & 0 \\ -\beta^*_L(E) & \alpha^*_L(E) & 0 \\ 0 & 0 & 1 \end{pmatrix}, \tag{5}$$

$$S_{H,\nu}(E) = \begin{pmatrix} 1 & 0 & 0 \\ 0 & \alpha_H(E) & \beta_H(E) \\ 0 & -\beta^*_H(E) & \alpha^*_H(E) \end{pmatrix}, \tag{6}$$

$$S_{H,\bar{\nu}}(E) = \begin{pmatrix} \bar{\alpha}_H(E) & 0 & \bar{\beta}_H(E) \\ 0 & 1 & 0 \\ -\bar{\beta}^*_H(E) & 0 & \bar{\alpha}^*_H(E) \end{pmatrix} \tag{7}$$

after omitting irrelevant phases. For this paper $S_{SI,\nu}(E)$ and $S_{SI,\bar{\nu}}(E)$ are treated as having identical structure to $S_{H,\nu}(E)$ and $S_{H,\bar{\nu}}(E)$ since the calculations for neutrino self-interactions, e.g. Duan *et al.* [23], use effective 2 flavor mixing. From $S_{H,\nu}(E)$, $S_{H,\bar{\nu}}(E)$, and $S_{L,\nu}(E)$ we define

$$P_L(E) = 1 - |\alpha_L(E)|^2 = |\beta_L(E)|^2, \tag{8}$$

$$P_H(E) = 1 - |\alpha_H(E)|^2 = |\beta_H(E)|^2, \tag{9}$$

$$\bar{P}_H(E) = 1 - |\bar{\alpha}_H(E)|^2 = |\bar{\beta}_H(E)|^2, \tag{10}$$

which are the crossing probabilities for neutrinos or antineutrinos at the two resonances. The resonances are said to be ''adiabatic'' or ''nonadiabatic'' depending upon whether the crossing probability is close to zero or closer to unity. Indeed these are the two natural values since the crossing probability is determined by the ratio of the resonance width to the local oscillation length scale and typically one is significantly larger than the other.

Our interest now turns to the initial states. The density at the proto-neutron star is so large that the matter eigenstates and the flavor eigenstates are strongly aligned there. Including neutrino self-interaction effects only makes the alignment stronger. From a full 3-neutrino mixing calculation we find that the initial matter basis spectra for a normal hierarchy (NH) are $\Phi_{\nu_3}(0, E) = \Phi_{\nu_e}(0, E)$, $\Phi_{\bar{\nu}_1}(0, E) = \Phi_{\bar{\nu}_e}(0, E)$ while all other states, $\Phi_{\nu_1}(0, E)$, $\Phi_{\nu_2}(0, E)$, $\Phi_{\bar{\nu}_2}(0, E)$, and $\Phi_{\bar{\nu}_3}(0, E)$ are equal to the $\Phi_{\nu_\mu}(0, E)$, $\Phi_{\nu_\tau}(0, E)$, $\Phi_{\bar{\nu}_\mu}(0, E)$, $\Phi_{\bar{\nu}_\tau}(0, E)$ spectrum which we call $\Phi_{\nu_x}(0, E)$. With an inverted hierarchy (IH) the initial states are $\Phi_{\nu_2}(0, E) = \Phi_{\nu_e}(0, E)$, $\Phi_{\bar{\nu}_3}(0, E) = \Phi_{\bar{\nu}_e}(0, E)$ and this time $\Phi_{\nu_1}(0, E)$, $\Phi_{\nu_3}(0, E)$, $\Phi_{\bar{\nu}_1}(0, E)$, and $\Phi_{\bar{\nu}_2}(0, E)$ are all equal to $\Phi_{\nu_x}(0, E)$. For the spectra exiting the neutrinosphere we adopt an ''alpha fit'' power law motivated both by its analytic simplicity and by recent supernova core Monte Carlo simulations [46]. For the time dependence of the luminosity we use an exponential decay with a time constant of $\tau = 3$ s. The differential spectra exiting the neutrinosphere follow

[1]Many of the profiles presented in Sec. II have multiple H resonances; therefore the matrices $S_{H,\nu}(E)$ and $S_{H,\bar{\nu}}(E)$ represent their combined effect of all the H resonances and $S_{L,\nu}(E)$ all the L resonances. We assume that the neutrinos encounter all L-type resonances after all H-type resonances. This is the case for all profiles we have generated.

$$\Phi_\nu(0,E,t) = \frac{L_\nu(\alpha+1)^{(\alpha+1)}}{\langle E_\nu\rangle^2\Gamma(\alpha+1)}\left(\frac{E}{\langle E_\nu\rangle}\right)^\alpha \times \exp\left[-(\alpha+1)\frac{E}{\langle E_\nu\rangle}\right]\exp[-t/\tau], \quad (11)$$

where L_ν is the luminosity, $\langle E_\nu\rangle$ the mean energy, and α is the "pinch" parameter. We employ a hierarchy of mean energies: $\langle E_{\nu_e}\rangle = 12$ MeV, $\langle E_{\bar\nu_e}\rangle = 15$ MeV, and $\langle E_{\nu_x}\rangle = 18$ MeV (where, again, x stands for either μ, τ, $\bar\mu$, or $\bar\tau$) and the luminosities are $L_{\nu_e} = L_{\bar\nu_e} = 6\times10^{52}$ erg/s, $L_{\nu_x} = 2\times10^{52}$ erg/s.

Putting the initial spectra and definitions of the S-matrices together one finds that the flux of matter state i a distance r from the supernova is given by

$$F_{\nu_i}(r,E) = \frac{1}{4\pi r^2}\sum_j |(S_\nu)_{ij}(E)|^2\Phi_{\nu_j}(0,E), \quad (12)$$

$$F_{\bar\nu_i}(r,E) = \frac{1}{4\pi r^2}\sum_j |(S_{\bar\nu})_{ij}(E)|^2\Phi_{\bar\nu_j}(0,E), \quad (13)$$

where $\Phi_{\nu_i}(0,E)$ and $\Phi_{\bar\nu_i}(0,E)$ are the initial spectra of the matter states. But what are detected at Earth are, of course, the flavor states. During their flight from the supernova to Earth any coherence between the matter eigenstates is lost so the flux of flavor α that arrives at Earth is the incoherent sum

$$F_{\nu_\alpha}(r,E) = \sum_i |U_{\alpha i}|^2 F_{\nu_i}(r,E). \quad (14)$$

These flavor fluxes may be rewritten in terms of the fluxes emitted by the neutrinosphere by introducing the survival probabilities $p(E)$ and $\bar p(E)$ for the electron neutrinos and antineutrinos, respectively, since these are the two flavors with distinct initial spectra. Written this way the detectable flavor fluxes are

$$F_{\nu_e}(r,E) = \frac{1}{4\pi r^2}[p(E)\Phi_{\nu_e}(0,E) + (1-p(E))\Phi_{\nu_x}(0,E)], \quad (15)$$

$$F_{\bar\nu_e}(r,E) = \frac{1}{4\pi r^2}[\bar p(E)\Phi_{\bar\nu_e}(0,E) + (1-\bar p(E))\Phi_{\nu_x}(0,E)], \quad (16)$$

$$4F_{\nu_x}(r,E) = \frac{1}{4\pi r^2}[(1-p(E))\Phi_{\nu_e}(0,E) + (1-\bar p(E))\Phi_{\bar\nu_e}(0,E) + (2+p(E) + \bar p(E))\Phi_{\nu_x}(0,E)], \quad (17)$$

where we have adopted the notation of Dighe and Smirnov [16] by denoting $F_{\nu_\mu} + F_{\nu_\tau} + F_{\bar\nu_\mu} + F_{\bar\nu_\tau}$ by $4F_{\nu_x}$. From Eqs. (12) and (13), and the initial spectra, we find that $p(E)$ and $\bar p(E)$ are related to the elements of $S(E)$ and $S_{\bar\nu}(E)$ via

$$p(E) = \sum_i |U_{ei}|^2 |(S_\nu)_{ij}(E)|^2, \quad (18)$$

$$\bar p(E) = \sum_i |U_{ei}|^2 |(S_{\bar\nu})_{ik}(E)|^2, \quad (19)$$

where $j=3$, $k=1$ for a normal hierarchy, and $j=2$, $k=3$ for an inverted hierarchy. After inserting the definition of the crossing probabilities and omitting the interference terms between the elements of $S_{SI,\nu}$ and $S_{H,\nu}$, $S_{SI,\bar\nu}$ and $S_{H,\bar\nu}$, the two survival probabilities $p(E)$ and $\bar p(E)$ are found to be

$$NH\begin{cases} p = (|U_{e1}|^2P_L + |U_{e2}|^2(1-P_L))(P_H(1-P_{SI}) + (1-P_H)P_{SI}) + |U_{e3}|^2(P_HP_{SI} + (1-P_H)(1-P_{SI})) \\ \bar p = |U_{e1}|^2(\bar P_H\bar P_{SI} + (1-\bar P_H)(1-\bar P_{SI})) + |U_{e3}|^2(\bar P_H(1-\bar P_{SI}) + (1-\bar P_H)\bar P_{SI}) \end{cases}, \quad (20)$$

$$IH\begin{cases} p = (|U_{e1}|^2P_L + |U_{e2}|^2(1-P_L))(P_HP_{SI} + (1-P_H)(1-P_{SI})) + |U_{e3}|^2(P_H(1-P_{SI}) + (1-P_H)P_{SI}) \\ \bar p = |U_{e1}|^2(\bar P_H(1-\bar P_{SI}) + (1-\bar P_H)\bar P_{SI}) + |U_{e3}|^2(\bar P_H\bar P_{SI} + (1-\bar P_H)(1-\bar P_{SI})) \end{cases}. \quad (21)$$

For clarity the energy dependence of all the probabilities has been suppressed. These formulae are quite general but from our knowledge of the various neutrino oscillation parameters we can be more specific about what exactly happens to the neutrinos and antineutrinos. The solar mixing parameters are such that the neutrino L resonance is almost completely adiabatic until, perhaps, the very end of the supernova neutrino signal. For this reason $P_L(E) = 0$. For the self-interaction probabilities we use an approximation [47] to the results reported by Duan *et al.* [23]. This approximation is

$$P_{SI}(E) = \Theta(E - E_C), \quad (22)$$

$$\bar P_{SI}(E) = 0, \quad (23)$$

where the step energy, E_C, is taken to be $E_C = 10$ MeV.

Thus at the end we find that determining the neutrino fluxes at Earth comes down to computing $P_H(E)$ or $\bar P_H(E)$. The Schrödinger equation forms a starting point by which $P_H(E)$ or $\bar P_H(E)$ can be determined. But if one naively applies, for example, a Runge-Kutta integrator to this equation one quickly discovers that this is a difficult problem from a numerical standpoint because such algorithms are simply not suited to differential equations where the solution is a highly oscillatory function. A number of alternate methods have been developed for calculating $P_H(E)$ or $\bar P_H(E)$, such as application of the Landau-

Zener result or the semianalytic method by Balantekin and Beacom [48], but for one reason or another these alternate approaches can break down for complex profiles. Some authors [27,49–51] have recognized that the evolution of the neutrino wave can be recast as a scattering problem and we adopt in this paper the algorithm outlined in Kneller and McLaughlin [27] which computes the evolution of the neutrino wave function by a Monte Carlo integration. For this paper we selected $|\delta m^2| = 3 \times 10^{-3}$ eV^2 and for θ_{13} we use $\sin^2\theta_{13} = 10^{-4}$ as a representative value. With this choice of θ_{13} the unperturbed profile is just sufficiently adiabatic to suppress the transformation effects of all but the most significant density features. The current experimental limit on θ_{13} is set by the CHOOZ experiment [52], and for our choice of δm^2 that limit is $\sin^2\theta_{13} < 0.1$.

Finally, in addition to the effects caused by the propagation through the supernova there are potentially Earth matter effects that can arise. These are straightforward to compute and we do not consider them here since their presence (or absence) in the neutrino signal is a function of the position of the supernova with respect to the detector when the event occurs.

IV. PROFILE FEATURES AND THE EFFECTS UPON THE CROSSING PROBABILITY

With the SN simulations complete and a method for calculating the crossing probabilities in hand we turn to study the effects of various features in the profiles upon P_H both as a function of time and energy.

A. The forward shock

The forward shock is a generic feature of all our SN simulations. Initially the shock is located close to the core and at high density and then, after it is regenerated, begins to move outwards and to lower densities as shown in the figures from Sec. II. In Fig. 12 we reproduce the results from Fig. 3 and also superimpose the resonance densities for 5, 10, 20, 40, and 80 MeV neutrinos. The radii where the horizontal dashed lines intercept the profile are the locations of the resonances, and in Fig. 13 we show P_H as a function of neutrino energy at six snapshots of this same simulation. The crossing probability as a function of the energy clearly evolves with time. If θ_{13} is not too small then the evolution of the neutrinos through the undisturbed progenitor profile is almost adiabatic, i.e. $P_H \sim 0$. As the forward shock arrives at the H-resonance for 5 MeV neutrinos—Fig. 12 indicates this occurs at shortly after $t \sim 1.8$ s—the evolution becomes nonadiabatic, i.e. $P_H \sim 1$ because the density jump across the shock straddles the resonance density of this neutrino energy. As time progresses and the shock moves outwards to lower densities we see from Fig. 12 that the shock will begin to affect 40 MeV neutrinos at $t = 3.6$ s. The nonadiabaticity sweeps up through the neutrino spectrum from low energy to high. As time progresses further eventually the shock

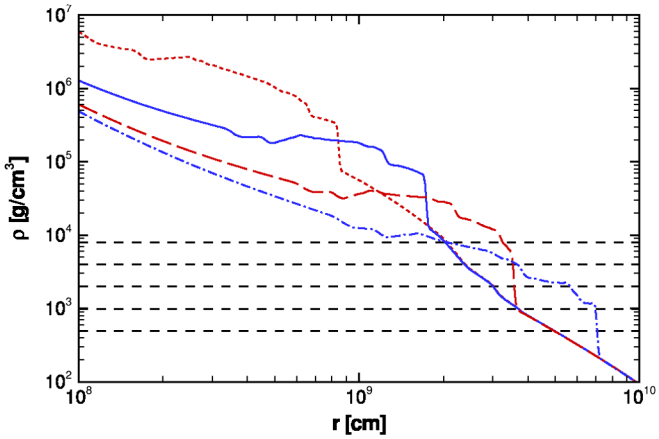

FIG. 12 (color online). The density as a function of the radius in a 1D SN model with $Q = 1.66 \times 10^{51}$ erg at $t = 0.9$ s (dotted line), $t = 1.8$ s (solid line), $t = 3.6$ s (long dashed line), and $t = 7.2$ s (dash-dot line). The horizontal dashed lines are (from top to bottom) the resonance densities for 5, 10, 20, 40, and 80 MeV neutrinos.

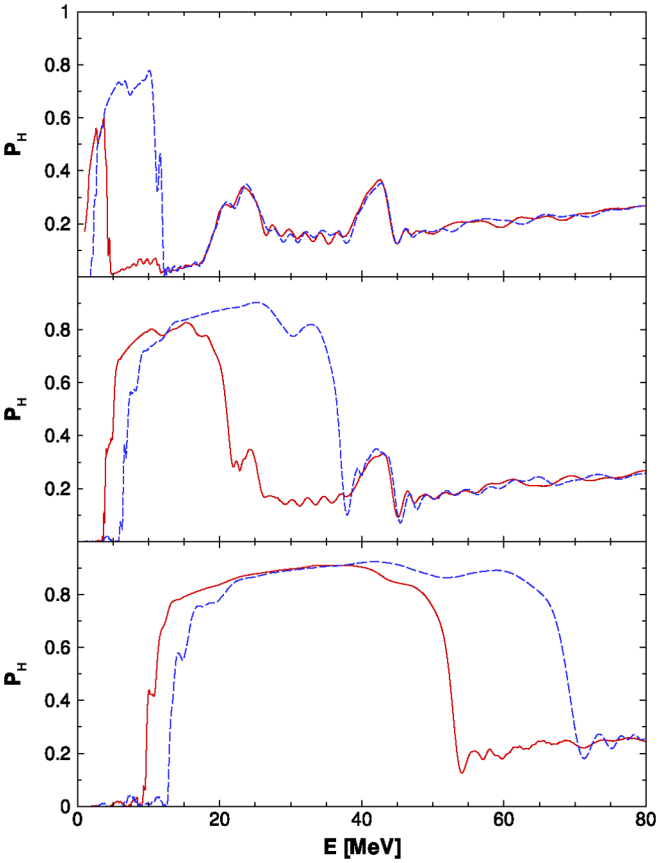

FIG. 13 (color online). The H resonance crossing probability P_H as a function of neutrino energy for the 1D SN simulation with $Q = 1.66 \times 10^{51}$ erg. In the top panel the snapshot times are $t = 2$ s (solid line) and $t = 2.5$ s (dashed line), in the middle panel $t = 3$ s (solid line) and $t = 3.5$ s (dashed line), and in the bottom panel $t = 4$ s (solid line) and $t = 4.5$ s (dashed line).

ceases to affect the neutrinos of a particular energy and so their propagation returns to being adiabatic. For this simulation Fig. 12 indicates that the evolution of 5 MeV neutrinos returns to being adiabatic at around $t = 3.6$ s and that for 40 MeV the return occurs roughly at $t = 7.2$ s. Note that the 5 MeV neutrinos were affected for a much briefer period (~ 1.8 s) than the 40 MeV neutrinos (~ 3.6 s). This is due to the shape of the density profile. A complimentary perspective is to look at how particular neutrino energies evolve with time such as those in Fig. 14. The temporary transition to nonadiabaticity for each neutrino energy is clearly visible in the figure. This figure makes it most obvious that the lower energies are affected before the higher and also that the duration of the nonadiabatic period increases with the neutrino energy.

The extent of the shock feature in neutrino energy seen in Fig. 13 is related to the density jump, $\Delta\rho$, across the shock. At any given time, if E_S is the highest neutrino energy affected by the shock and ΔE is the range of neutrino energies then the density jump across the shock is

$$\frac{\Delta\rho}{\rho} = \frac{\Delta E}{E_S - \Delta E}, \tag{24}$$

which is independent of the mixing parameters. From Eq. (3) we saw that, for normal shocks, $\Delta\rho$ is a function of the Mach number and ratio of specific heats γ. If M is large then $\Delta\rho$, and consequently ΔE, are essentially just a function of γ but if the Mach number M is not too large—which may be the case—then the width of this feature could be used to infer M if γ is known. As the SN proceeds to explode E_S moves up through the neutrino spectrum. The correspondence between energy and resonance density means that if we know, or assume, a progenitor profile shape then E_S measures the shock position r_S. From the locations of E_S shown in Fig. 13, and the initial profile, we show in Fig. 15 r_S as function of time for this particular simulation. The change of r_S with time of course measures the shock speed but we can also use $r_S(t)$ to extrapolate the shock position both forward in time, if necessary, but, more interestingly, also backwards toward the proto-neutron star. If this extrapolation can be accomplished successfully then we can infer the moment, t_{200}, when $r_S \sim 200$ km. The neutronization burst (if detected) supplies a zero of time so $t_{200} \neq 0$ is the brief period the shock was stalled. Thus the neutrino signal, and, in particular, the location of the forward shock, contains evidence of whether a key component of the core-collapse supernova paradigm is correct and can provide quantitative data with which to compare with more sophisticated SN simulations than ours. We illustrate this idea in Fig. 15 where we have artificially included an offset in time.

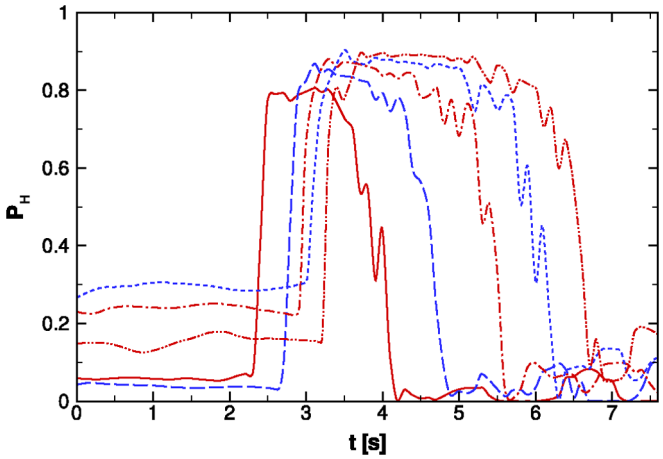

FIG. 14 (color online). The H resonance crossing probability P_H as a function of time for selected neutrino energies through the 1D SN model with $Q = 1.66 \times 10^{51}$ erg. The curves are: $E = 10$ MeV (solid line), $E = 15$ MeV (long dashed line), $E = 20$ MeV (dash-dot line), $E = 25$ MeV (short dashed line), and $E = 30$ MeV (dash double-dot line).

B. The reverse shock

The reverse shock was a feature seen in the more powerful explosions from Sec. II and the 2D result. This feature was not present in the initial profile and appeared later on when the velocity of the wind superseded the local sound speed. After its formation the reverse shock initially moved outwards into the star but, as the energy deposition faded with time and the strength of the wind abated, eventually the reverse shock stalled and then headed back to the core. Like the forward shock, the reverse shock affects the adiabaticity of the evolution of the neutrino wave function through the profile so that neutrinos with resonance densities straddled by the density jump across the reverse shock evolve nonadiabatically as they pass through it. Note that any neutrino with a resonance density straddled by the density jump across the reverse shock will also experience two other resonances: one before the reverse shock and one after. This is shown in Fig. 16 where we

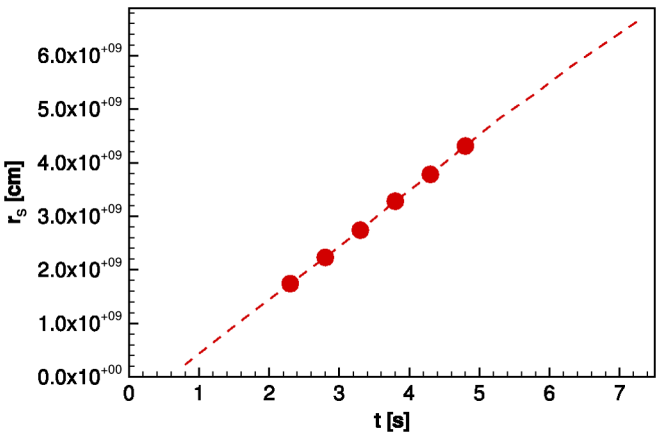

FIG. 15 (color online). The shock position as a function of time, $r_s(t)$, for the 1D SN simulation where $Q = 1.66 \times 10^{51}$ erg. An artificial time delay of 500 ms has been added to mimic the stalling of the shock at $r_S \sim 200$ km.

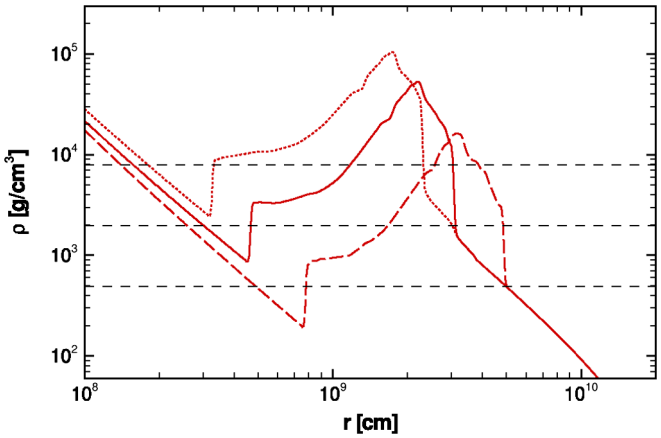

FIG. 16 (color online). The density as a function of the radius in a 1D SN model with $Q = 4.51 \times 10^{51}$ erg at $t = 1.0$ s (dashed line), $t = 1.5$ s (solid line), and $t = 2.0$ s (long dashed line). The horizontal dashed lines are (from top to bottom) the resonance densities for 5, 20, and 80 MeV neutrinos.

have superimposed the resonance densities for 5, 20, and 80 MeV neutrinos upon the profiles shown in Fig. 6. We see from the figure that it is possible for some neutrinos to be affected by both shocks. If this occurs, and if we neglect the effects from other resonances in the profile, then we might expect that the net effect upon such doubly shock-affected neutrinos to be zero [37,42]. However this expected cancellation is not seen in our results for P_H as a function of the neutrino energy shown in Fig. 17 for the model where $Q = 3.36 \times 10^{51}$ erg. The crossing probabilities plotted in the figure show some similarities to those plotted in Fig. 13 at the higher neutrino energies affected by the forward shock where there is change from adiabatic to nonadiabatic evolution. But for those energies where cancellation is naively expected we see instead that P_H oscillates wildly. These rapid oscillations are phase effects due to the interference between the two shocks. Similar rapid oscillations in the crossing probability have been seen previously in SN neutrino calculations by Fogli *et al.* [36] in a profile with a forward shock and then a bubble cavity behind it, in the SN test case used by Kneller and McLaughlin [27], and in the results of Dasgupta and Dighe [28] where their significance was emphasized.

In Fig. 18 we display the crossing probability for the model where $Q = 4.51 \times 10^{51}$ erg at $t = 1.1$ s, $t = 1.4$ s, and $t = 3.0$ s. Again phase effects are seen. Compared to the results shown in Fig. 17 for the weaker explosion where $Q = 3.36 \times 10^{51}$ erg and in Fig. 15 for $Q = 1.66 \times 10^{51}$ erg, in this case there is no indication of the characteristic transition from adiabatic to nonadiabatic propagation associated with the forward shock. This occurs because, as noted earlier about this model, the reverse shock penetrates to lower densities than the forward shock at these early times. For this particular model the reverse shock affects the adiabaticity of a particular neutrino energy before the forward shock.

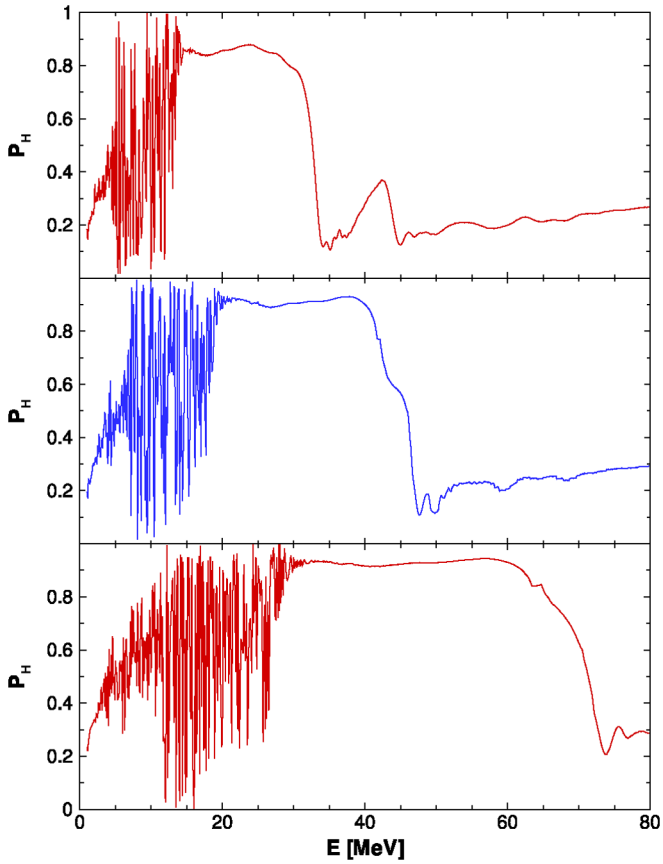

FIG. 17 (color online). The H resonance crossing probability P_H as a function of neutrino energy for three snapshots taken from the 1D SN model where $Q = 3.36 \times 10^{51}$ erg. In the top panel the time is $t = 1.8$ s, in the middle $t = 2.0$ s, and in the bottom panel $t = 2.4$ s.

The presence of phase effects in P_H are caused by interference between forward and reverse shocks. But it would be nice to find in the neutrino signal a clean signature of the reverse shock that is not contaminated by the forward shock or other features of the profile. A potential signature could arise from the behavior noted earlier which is that the reverse shock stalled as the energy deposition into the material above the proto-neutron star faded and then headed back towards the core. As the reverse shock moves backwards its effects move down through the neutrino spectrum and might eventually cease to overlap with the forward shock. Since the density jump across the reverse shock becomes quite small by the time this behavior occurs the reverse shock will produce a narrow spectral feature. For the simulation where $Q = 3.36 \times 10^{51}$ erg, shown in Fig. 5, this expected pattern is difficult to see in the neutrino signal because the forward shock has not swept through the neutrino spectrum by the time the reverse shock turns around. But in the simulation with slightly larger energy deposition, $Q = 4.51 \times 10^{51}$ erg, the forward shock moves much more quickly and has largely swept through the H resonance region by the

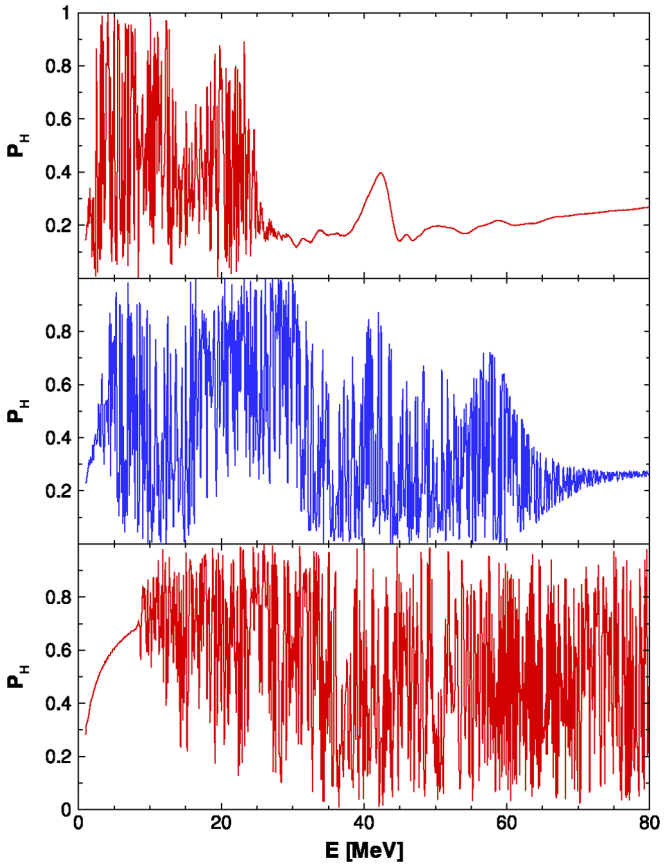

FIG. 18 (color online). The H resonance crossing probability P_H as a function of neutrino energy for three snapshots taken from the 1D SN model where $Q = 4.51 \times 10^{51}$ erg. In the top panel the time is $t = 1.1$ s, in the middle $t = 1.4$ s, and in the bottom panel $t = 3.0$ s.

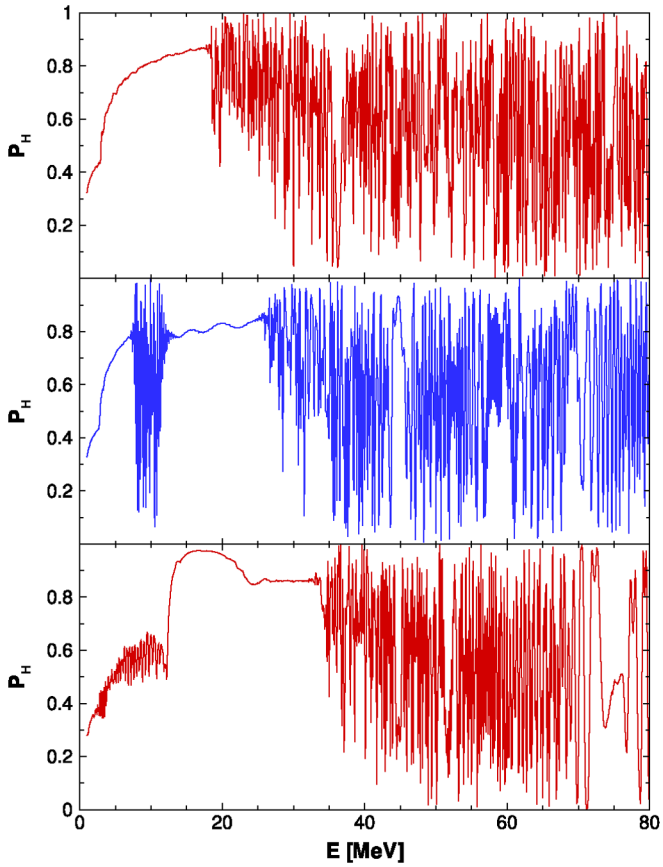

FIG. 19 (color online). The H resonance crossing probability P_H as a function of neutrino energy for the 1D SN model where $Q = 4.51 \times 10^{51}$ erg. From top to bottom the snapshot times are $t = 4$ s, $t = 4.5$ s, and $t = 4.9$ s.

time the reverse shock starts to make its way back to the core. For this simulation the backwards moving reverse shock is more visible in the neutrino signal. The crossing probability for this simulation at the snapshots shown in Fig. 8 are presented in Fig. 19. The backwards moving reverse shock is responsible for the phase effects at $E_\nu \sim 10$ MeV in the middle panel. Then once the reverse shock has reached the core our boundary conditions there led to its reflection and so the reverse shock became an outward moving, weak forward shock and reappeared in the neutrino spectrum as a spectral feature moving from low to high neutrino energies. This is the cause of the bump in P_H seen at $E_\nu \sim 15$-20 MeV in the bottom panel.

In summary, though it is apparent that the neutrino signal can vary considerably depending upon exactly how the reverse shock behaves, the presence of strong phase effects—rapid oscillations with large amplitude in both time and energy of the crossing probability—are a notable signature of the presence of multiple shocks. Therefore, there exists tremendous potential in a future detection of a supernova neutrino signal for probing the inner hydrodynamics of the explosion.

C. Asphericity

The notable difference between the one-dimensional and the two-dimensional models was the local density fluctuations that appeared in the latter. These local density enhancements/cavities affect only neutrinos along particular lines of sight so if one could determine their presence in the signal we would obtain an indication of the asphericity of the explosion. The most obvious method would be to compare different lines of sight to the same SN but obviously this is not practical. Instead we must find another signature of asphericity that one might use. In Fig. 20 we show the crossing probability P_H as a function of neutrino energy for the snapshot $t = 2.4$ s, $t = 5.4$ s, and $t = 6.4$ s and a line of sight $\theta = 25°$. Features in the figure resemble those seen in the 1D results: the forward shock leads to a range of energies with $P_H \rightarrow 1$ as seen in the top panel, phase effects due to presence of the reverse shock lead to the high "frequency" oscillations of P_H seen in the middle panel, and the turn around of the reverse shock can be seen in the bottom panel at $E \sim 15$ MeV where it appears, as before, as a narrow range of high frequency phase effects moving down through the spectrum. While a detailed analysis of these results might indicate a difference that

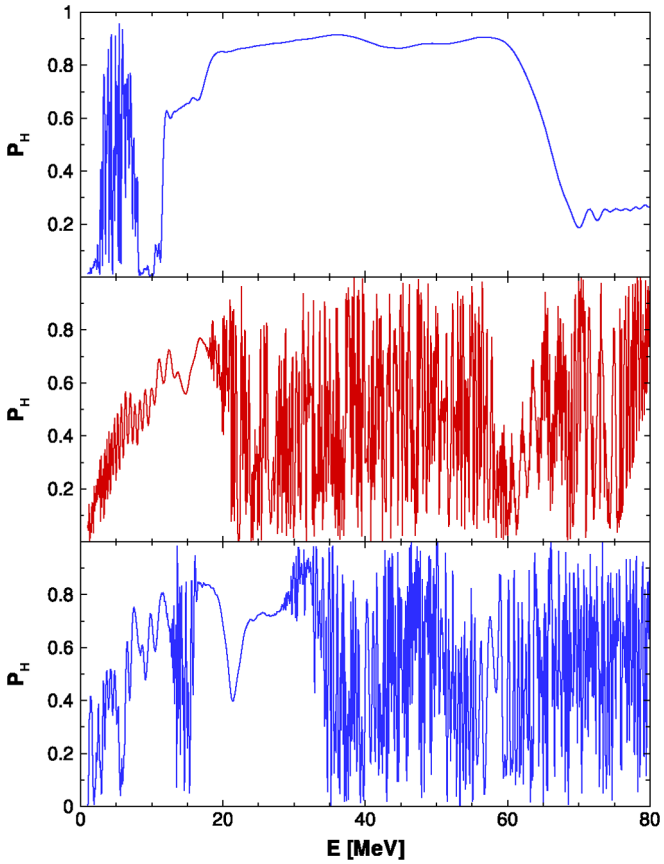

FIG. 20 (color online). The H resonance crossing probability P_H as a function of neutrino energy for a radial slice at $\theta = 25°$ through the 2D SN model. From top to bottom the snapshot times are $t = 2.4$ s, $t = 5.4$ s, and $t = 6.4$ s.

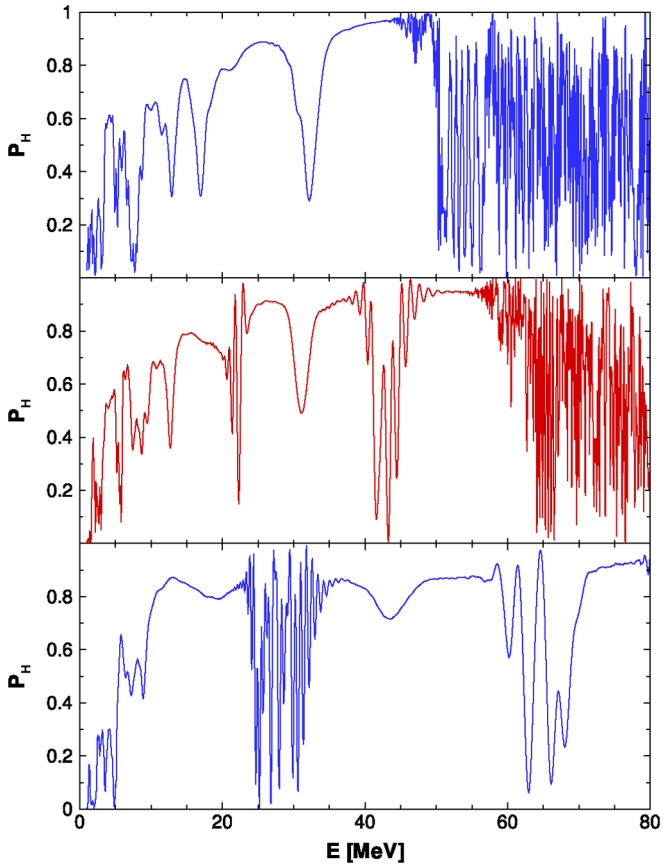

FIG. 21 (color online). The H resonance crossing probability P_H as a function of neutrino energy for a radial slice at $\theta = 25°$ through the 2D SN model. From top to bottom the snapshot times are $t = 7.4$ s, $t = 8.0$ s, and $t = 9.0$ s.

is due to asphericity there is no striking feature that one can point to. However, at late times we found a change in the qualitative appearance of P_H versus neutrino energy. The high frequency phase effects no longer dominate the entire spectrum and now lower frequency portions show up. We did not see anything comparable at late times in any of our 1D simulation results. The changing quality of the phase effects are seen in Fig. 21 which shows the crossing probability at the H resonance as a function of neutrino energy for the same line of sight at $\theta = 25°$ through the 2D model. High frequencies can be seen above $E \sim 45$ MeV in the top panel and above $E \sim 55$ MeV in the middle panel but they have disappeared by $t = 9.0$ s. In all three panels we see that at lower neutrino energies the curve is smoother with only narrow patches of high frequency phase effects that moved up through the spectrum. The shocks have largely ceased affecting the lower neutrino energies by this time so it is the "fluctuations" upon the profile—both between the shocks and behind the reverse shock—which produce mildly adiabatic resonances, and/or resonances that are located very close to one another (and possibly even overlap) that give rise to these features in the figure.

The effect upon neutrino flavor transport of supernovae density fluctuations was considered by Loreti *et al.* [53] and later by Fogli *et al.* [54], Friedland and Gruzinov [55], and Choubey, Harries, and Ross [56]. These authors suggest that P_H should tend to $1/2$ in the presence of many small scale fluctuations. We note, however, that due to the exponential growth of the radial grid spacing the scale of features we can resolve by $r \sim 10^4$ km-10^5 km is of order $\delta r \sim 100$ km and this is somewhat larger than the scales considered by Fogli *et al.*, Friedland and Gruzinov, and Choubey, Harries, and Ross. In our formulation of neutrino mixing using S-matrices we can motivate this expected result of $P_H \rightarrow 1/2$ by dividing the density profile into domains such that within each there is a single neutrino resonance. The passage of a neutrino (or antineutrino) through each interval is described by an S-matrix which has exactly the same structure as Eqs. (6) or (7) as appropriate. The magnitudes of the elements α and β lie between zero and unity depending upon the adiabaticity of the resonance in that region. The multiplication of all these S matrices together (in the correct order) to achieve the net effect of passing through all the resonances will tend to produce a net result where either α_H and β_H or $\bar{\alpha}_H$ and $\bar{\beta}_H$

are of equal magnitude. In our simulations we had cases where we found up to 13 resonances but have not been able to reproduce the anticipated limiting behavior. Nevertheless, as shown in Figs. 20 and 21, we see a clear distinctive qualitative change in the crossing probabilities at late time in aspherical models.

V. DETECTOR SIGNALS

Since the detection of neutrinos from SN 1987A in IMB [57] and Kamiokande [58] the number and size of the neutrino detectors have both increased in scale so that many thousands or even tens of thousands of neutrinos will be detected from the next galactic supernova. Though many neutrino detectors are water Cerenkov detectors that are best suited to detecting the electron antineutrinos from supernovae via the inverse-β reaction on protons, other neutrino detection technologies have been demonstrated or explored that allow one to see the electron neutrinos and the μ/τ flavors via nucleus-neutrino reactions such as $O(\nu_e, e)F$, or neutral current reactions such as $D(\nu_X, \nu_X)np$. The detection of these other neutrino flavors would provide a great deal of valuable information we could then use to learn about the SN explosion. A heavy water detector is sensitive to both charged-current and neutral-current events so it could be used to detect the μ and τ flavors. However obtaining energy resolution for the neutral current events is difficult so the observable quantity considered by Schirato and Fuller [34] was the ratio of total charged-current to neutral-current events. Though temporal evolution of this ratio is somewhat smothered due to the fact that the event rates are integrated over the neutrino spectrum, Schirato and Fuller demonstrated that variations of the ratio would occur at the level of 10%–20%. Lead detectors are also capable of detecting the μ/τ flux and have been studied by Fuller, Haxton, and McLaughlin [15], Engel, McLaughlin, and Volpe [17], and Kolbe *et al.* [59].

For the purposes of demonstrating the temporal evolution of supernovae neutrino signals we shall consider just those of the water Cerenkov detector variety because the majority of neutrino detectors are of this type. These detectors are sensitive to both electron neutrinos and electron antineutrinos via the reactions $p(\bar{\nu}_e, \bar{e})n$ and $O(\nu_e, e)F$ [60] with the inverse-β reaction dominating the signal. The cross sections for the neutrino-nucleon reactions are well known but a good deal of uncertainty exists in the important neutrino-nucleus cross sections.

To determine what any given detector will see we must put together four components: the initial neutrino spectra emitted by the proto-neutron star, the effects upon the neutrinos of passage through the SN, the energy dependence of the cross sections in the detector and, fourthly, the energy resolution of the detector. The first two parts have already been dealt with so we need only focus upon the flux that arrives at Earth and the detector response. To see the temporal variations of the neutrino signal we have been discussing in a water Cerenkov detector would require an inverted hierarchy but we shall postpone restricting ourselves to just this scheme until we present the positron spectra.

A. The neutrino flux at Earth

The actual neutrino flux of a particular flavor through a detector differs from that emitted from the neutrinosphere. Calculating this change is the focus of our paper and is described in detail in Sec. IV. In the simplest scenario, if the neutrinos propagate through the outer layers of the SN adiabatically then the survival probabilities p and $\bar{p}$ are found by setting $P_H = P_L = \bar{P}_H = 0$ in Eqs. (20) and (21). For the normal hierarchy then $p(E) = |U_{e2}|^2\Theta(E - E_C) + |U_{e3}|^2\Theta(E_C - E)$ and $\bar{p} = |U_{e1}|^2$: for the inverse hierarchy $p(E) = |U_{e2}|^2\Theta(E_C - E) + |U_{e3}|^2\Theta(E - E_C)$ and $\bar{p} = |U_{e3}|^2$. Using the value of $\sin^2 2\theta_{13} = 4 \times 10^{-4}$ we used to calculate P_H and $\sin^2 2\theta_{12} = 0.8$ based upon the solar mixing parameters, we see that for the normal hierarchy and $E < E_C$ the amount of the emitted ν_e flux present in the electron neutrino flux at a detector here on Earth is minuscule while for $E > E_C$ it is around 28%. For an inverted hierarchy the situation is flipped with $p = 28\%$ for $E < E_C$ and $p = 10^{-4}$ for $E > E_C$. With the same mixing angle values we find $\bar{p} = 72\%$ of the emitted electron antineutrino flux present in the electron antineutrino flux at Earth in a normal hierarchy but only $\bar{p} = 10^{-4}$ for an inverted hierarchy.

The evolution of the density profile alters our expectations. Depending upon the scenario, either p (for a normal hierarchy) or $\bar{p}$ (for an inverted hierarchy) will change with time and so the proportions of the emitted fluxes present in the fluxes at Earth will also change. Note that p and $\bar{p}$ do not both evolve with time within the same scenario; one will stay constant. This means there is a potential to separate the time evolution of the emitted flux from the neutrinosphere from the evolution of the density profile through which the neutrinos propagate. As the star explodes and the forward shock eventually reaches the H resonances the passage of portions of the neutrino spectrum through the density profile becomes nonadiabatic, i.e. $P_H = 1$ for the NH or $\bar{P}_H = 1$ for the IH. When this occurs the electron neutrino survival probability changes to $p(E) = |U_{e2}|^2\Theta(E_C - E) + |U_{e3}|^2\Theta(E - E_C)$ for the normal hierarchy while the electron antineutrino survival probability switches to $\bar{p} = |U_{e1}|^2$ when the hierarchy is inverted.

In Figs. 22 and 23 we present the neutrino flux at Earth from a SN at a distance of 10 kpc if the evolution were either completely adiabatic or completely nonadiabatic, i.e. $P_H = 0$ or $P_H = 1$, and $\bar{P}_H = 0$ or $\bar{P}_H = 1$, in either the normal or inverted hierarchy. The two curves in each panel of the figures therefore represent extremes in the sense that the actual flux at a given energy would fall somewhere in between the two curves. We do not plot

the electron antineutrino flux for the normal hierarchy or the electron neutrino flux for the inverted hierarchy because they cannot change due to the evolving density profile. In each panel of the two figures the pinch parameter was set to $\alpha = 3$: other than a change in shape the general behavior of the curves for other values of α is identical. There are many points to notice in each figure. The first is that the stepwise crossing of the spectra can be clearly seen at $E_C = 10$ MeV for all flavors bar the electron antineutrinos. There is also a noticeable distinction in the combined $\nu_\mu + \bar{\nu}_\mu + \nu_\tau + \bar{\nu}_\tau$ spectra of the two figures. And then, for any given neutrino flux and hierarchy there is a particular energy where the two curves cross. The crossing can be seen best in the ν_e spectrum in the normal hierarchy where it is located at around 28 MeV. We define the energies where the curves cross as the critical energies. The critical energies vary with both flavor, the hierarchy, and the chosen initial spectra. At the critical energy for a particular hierarchy and flavor the adiabaticity of the neutrinos as they propagate through the profile is irrelevant and the flux of that flavor and at that energy through a detector is independent of P_H. Another significant feature to notice is the large difference between the two curves for the electron neutrinos and electron antineutrinos for energies below $E \sim 30$ MeV. This wide separation of the extremal fluxes at low to medium neutrino energies, $E \lesssim 30$ MeV, suggests that we focus our attention upon this portion of the spectrum because it is here that changes in adiabaticity will lead to the most significant changes in the flux. The flux at higher energies will also change with the evolving adiabaticity but to a lesser degree because the fluxes are so small.

If the evolution of the neutrinos through the density profile were always adiabatic then p and $\bar{p}$ would be constant in time and the composition of the fluxes at Earth in terms of the emitted spectra would not change. Depending upon the hierarchy and the threshold energy of the detector it may be very difficult to pick out the small amounts of the emitted $\nu_e/\bar{\nu}_e$ present in the detected $\nu_e/\bar{\nu}_e$ flux. In such cases we would need to detect the ν_μ, $\bar{\nu}_\mu$, $\bar{\nu}_\tau$, and/or ν_τ flavors to properly see the ν_e or $\bar{\nu}_e$ spectrum that

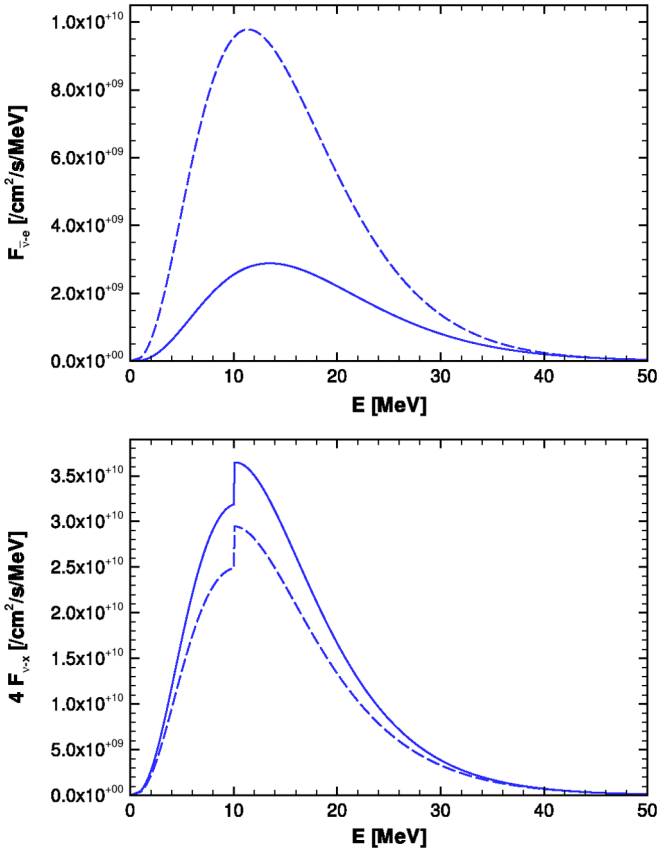

FIG. 22 (color online). Fluxes of electron antineutrinos (top panel) and the sum of $\nu_\mu + \bar{\nu}_\mu + \nu_\tau + \bar{\nu}_\tau$ neutrino fluxes (bottom panel) for completely adiabatic, i.e. $P_H = 0$ (solid line) and nonadiabatic, i.e. $P_H = 1$ (dashed line) evolution. The hierarchy is inverted, the pinch parameter was set to $\alpha = 3$ and the vacuum mixing angles are $\sin^2(2\theta_{12}) = 0.8$, $\sin^2(2\theta_{13}) = 4 \times 10^{-4}$. The distance to the SN was set at $d = 10$ kpc and the time t to $t = 0.0$ s.

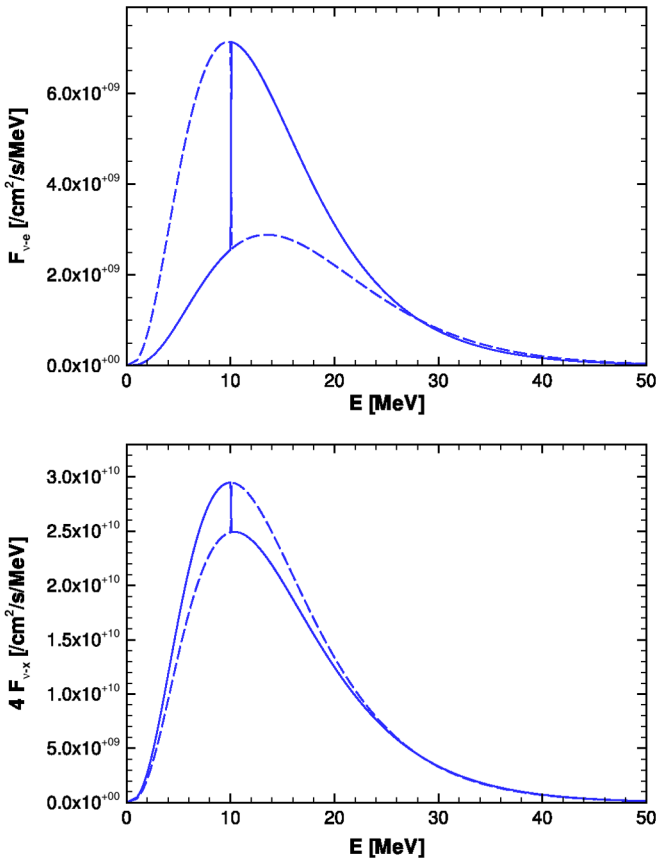

FIG. 23 (color online). The fluxes of electron neutrinos (top panel) and the sum of $\nu_\mu + \bar{\nu}_\mu + \nu_\tau + \bar{\nu}_\tau$ neutrino fluxes (bottom panel) for completely adiabatic, i.e. $P_H = 0$ (solid line) and nonadiabatic, i.e. $P_H = 1$ (dashed line) evolution. Here the hierarchy is normal but otherwise all parameters are the same as those used in Fig. 22.

was originally emitted from the proto-neutron star. But when the evolution of the neutrinos becomes nonadiabatic due to the effects of the evolving density profile the composition of the ν_e or $\bar{\nu}_e$ flux at Earth (in terms of the emitted spectra) is altered. The explosion acts like a window sweeping across either the neutrino or antineutrino spectra through which we observe an altered mixture of the emitted components allowing us to get at information about the emitted spectra that was otherwise hidden from view.

B. Cross sections and energy resolution

In a water Cerenkov detector there are two parts to the signal: the positrons emitted from the inverse β reactions and then the electrons released by $O(\nu_e, e)F$. We focus upon the positron spectrum because it is the dominant portion. The positron spectrum seen in a detector, $\Phi_{e^+}(E_{e^+})$, is given by

$$\Phi_{e^+}(E_{e^+}) = N_p \int dE_{\bar{\nu}_e} F_{\bar{\nu}_e} \frac{d\sigma}{dE_{e^+}}, \tag{25}$$

where N_p is the number of protons in the detector, $F_{\bar{\nu}_e}$ is the electron antineutrino flux, and $d\sigma/dE_{e^+}$ is the differential cross section. For our analysis we used the cross sections of Strumia and Vissanti [61]. We also need to consider the relationship between the neutrino energy and the positron energy and our ability to resolve the features of the neutrino spectrum. The positron energy and neutrino energy are closely correlated as shown in Fig. 24. Features in the neutrino spectrum at a particular energy will appear in the positron spectrum at more or less the same energy. But the positron spectrum is smoothed relative to the neutrino spectrum by two effects: the distribution of positron energies for a given neutrino energy, and the energy resolution of the detector. For a given neutrino energy the positrons emerge with a range of energies which

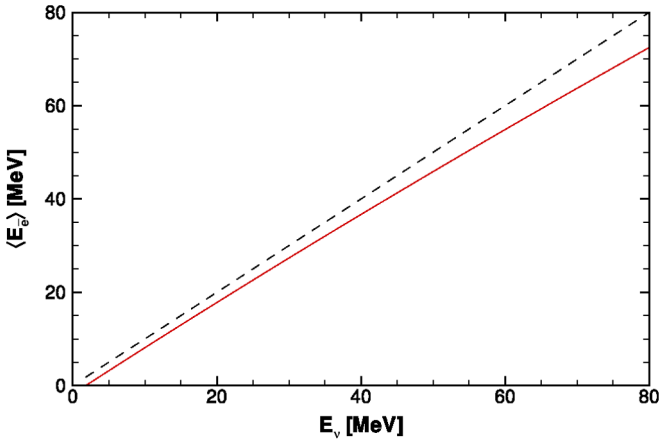

FIG. 24 (color online). The "mean" positron energy $\langle E_{\bar{e}} \rangle$ as a function of the neutrino energy (solid line) given by Eq. (16) in Strumia and Vissanti [61]. The dashed line is $\langle E_{\bar{e}} \rangle = E_\nu$.

we may invert so that for a given positron energy, E_{e^+}, there is a range of neutrino energies, Δ, from which it could have arisen. This range[2] is given by

$$\Delta = \frac{m_n^2 - m_p^2 - m_e^2 + 2m_p E_{e^+}}{2} \left(\frac{1}{m_p - p_{e^+} - E_{e^+}} - \frac{1}{m_p + p_{e^+} - E_{e^+}} \right), \tag{26}$$

where p_{e^+} is the momentum of the positron and m_n, m_p, and m_e are the masses of the neutron, proton, and electron, respectively. Δ is shown in Fig. 25 as a function of the positron kinetic energy. Then for the energy resolution of the detector we used a filter so that the spectrum of positrons at energy E_{e^+} is given by

$$\Phi(E_{e^+}) = \frac{\int dE'_{e^+} \Phi(E'_{e^+}) W(E_{e^+}|E'_{e^+})}{\int dE'_{e^+} W(E_{e^+}|E'_{e^+})} \tag{27}$$

and we take $W(E_{e^+}|E'_{e^+})$ to be a normalized Gaussian with a mean E'_{e^+} and a variance $\sigma^2(E'_{e^+})$ given by

$$\frac{\sigma}{E_{e^+} - m_e} = 0.319 \left(\frac{1}{E_{e^+} - m_e \ [\mathrm{MeV}]} \right)^{0.3467}. \tag{28}$$

This formula is our fit to the energy resolution of the Super-K detector [62]. The energy resolution of the detector, σ, is also shown in Fig. 25 as a function of the positron kinetic energy. Both smearing effects, the range, Δ, of neutrino energies that can produce a positron with energy E_{e^+}, and the detector resolution, σ, increase with E_{e^+} and we notice that beyond $E_{e^+} \sim 40$ MeV it is the range Δ that determines the scale of the features we can resolve. Below $E_{e^+} \sim 40$ MeV the detector resolution limits our ability to see features of the neutrino spectrum.

Finally we should mention that for this paper we do not consider the Poisson error due to the finite number of detected events. This effect does not smooth out features of the spectrum so much as make them difficult to detect. The Poisson error scales with the size of the detector and also depends upon the chosen energy and temporal bin sizes. For these reasons we shall postpone the inclusion of the Poisson noise for another time.

C. The positron spectra

The positron spectrum allows us to see the effect of the density profile upon the neutrino flux. In Fig. 26 we plot the positron spectrum convolved with our adopted detector energy resolution as a function of positron energy for the weakest 1D simulation, $Q = 1.66 \times 10^{51}$ erg, and an inverted hierarchy. The shock can be seen, beginning at $E \sim 5$ MeV at $t \sim 2$ s and ending at $E \sim 35$ MeV at $t \sim 3.5$ s, as the discontinuity moving up through the spectrum.

[2]The formula is valid for positron energies such that $p_{e^+} + E_{e^+} \leq m_p$.

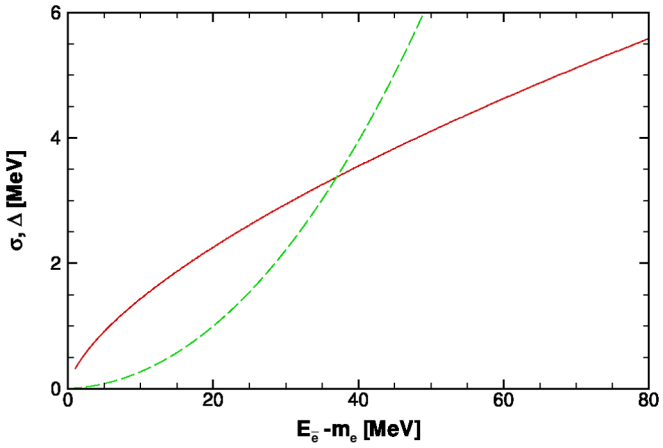

FIG. 25 (color online). The Super-K energy resolution error, σ, (solid line) and the range of positron energies, Δ, (dashed line) as a function of the positron kinetic energy.

There is a distinct curvature to the discontinuity locus that is due to a combination of the progenitor profile and the shock speed. The backside of the shock can also be seen, beginning at $E \sim 5$ MeV at $t \sim 4$ s and ending at $E \sim 30$ MeV at $t \sim 7$ s, but it is a less noticeable feature. This line through the figure is also curved but not to the same extent as the front of the shock. Given enough events even present detector technology would allow us to see the shock move up through the positron spectrum from which we could begin to glean information about the explosion.

If we take slices through Fig. 26 then we produce Fig. 27 in which we plot the positron spectrum as a function of time at $E = 10$ MeV, $E = 20$ MeV, and $E = 30$ MeV.

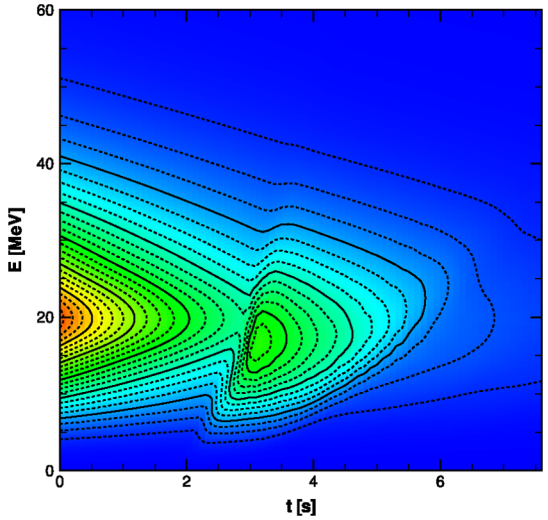

FIG. 26 (color online). The positron spectrum per unit time and per unit tonne of detector as a function of energy and time for the 1D simulation with a total energy deposition of $Q = 1.66 \times 10^{51}$ erg and convolved with our adopted detector energy resolution. The neutrino hierarchy is inverted. The solid contours are linearly spaced by 10^{-3}/MeV/s/t.

The general trend for each positron energy shown is $\propto \exp(-t/\tau)$ since this was the time dependence we used for the emitted spectra but upon this exponential decay the shock is obviously visible for all three chosen energies in both filtered and unfiltered curves. The width of the forward shock feature grows with E as we noted earlier as the front of the shock accelerates more quickly through the neutrino spectrum than the back.

In Fig. 28 we plot the positron spectrum convolved with the adopted detector resolution for the more powerful explosion with $Q = 3.36 \times 10^{51}$ erg as a function of time and energy. Compared to Fig. 26 the contours are not as smooth but, nevertheless, the shock can be seen again as a sharp discontinuity in the contours; but now, because of the more energetic explosion and faster shock velocity, disturbance of the evolution of the neutrinos begins at $t \sim 1$ s and has swept entirely through the spectrum by $t = 2$ s. The shock discontinuity is noticeably more vertical than for the $Q = 1.66 \times 10^{51}$ erg model shown in Fig. 26 which is, again, indicative of the faster shock speed. Interestingly we notice a pulse in the positron spectrum at $t \sim 3.5 - 4$ s which is around the same time when the reverse shock, after stalling and returning to the core, reaches the H resonance again as a weak forward shock as shown in Fig. 7.

The presence of the reverse shock is much clearer when we examine Fig. 29 for the yet more powerful $Q = 4.51 \times 10^{51}$ erg 1D explosion. Again the shock makes an appearance as a break in the contours at $t \sim 1$ s starting at low energy and racing up through the spectrum but we also notice a distinct V-shaped break in the contours between $t = 4$ s and $t = 5$ s. This time period is exactly when the reverse shock stalled, headed back to the core whereupon it was reflected and propagated outwards again as a weak

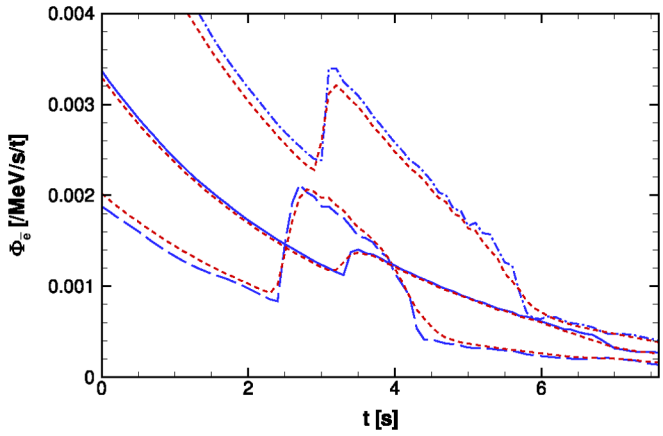

FIG. 27 (color online). The positron spectrum in the case of the inverted hierarchy per unit tonne of detector as a function of time at various positron energies for the 1D simulation with a total energy deposition of $Q = 1.66 \times 10^{51}$ erg. The curves are $E = 10$ MeV (long dashed line), $E = 20$ MeV (dash-dot line), and $E = 30$ MeV (solid line). The short dashed lines indicate the spectrum convolved with our adopted detector energy resolution.

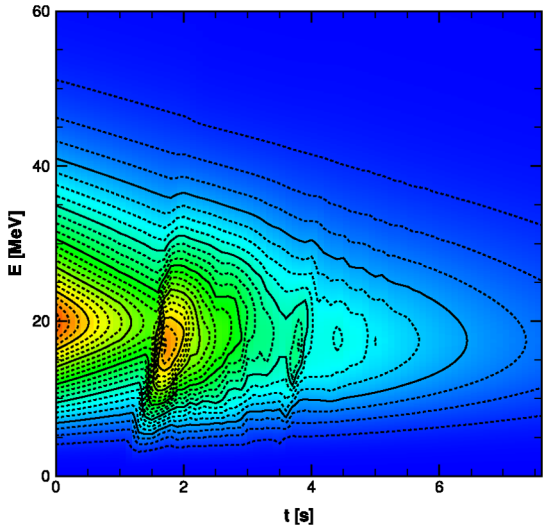

FIG. 28 (color online). The convolved positron spectrum per unit time and per unit tonne of detector as a function of energy and time for the 1D simulation with a total energy deposition of $Q = 3.36 \times 10^{51}$ erg and an inverted neutrino hierarchy. The solid contours are evenly spaced by 10^{-3}/MeV/s/t.

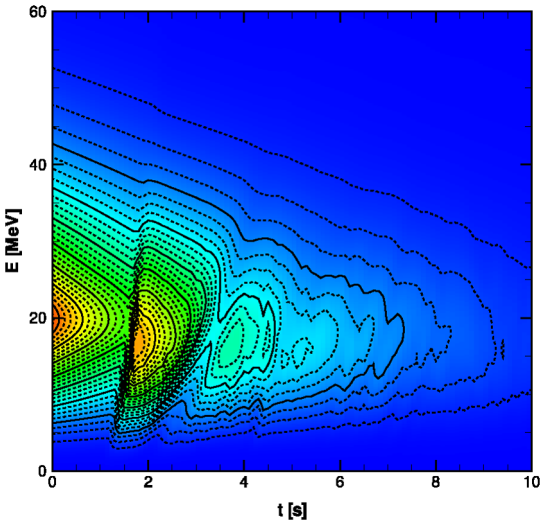

FIG. 30 (color online). The positron spectrum per unit time and per unit tonne of detector as a function of energy and time for the 2D simulation and convolved with our adopted detector energy resolution. The solid contours are linearly spaced by 10^{-3}/MeV/s/t.

forward shock. The behavior of the reverse shock over this time period was shown in Fig. 8.

Finally in Fig. 30 we plot the positron spectrum for the 2D simulation as a function of time and energy. The forward shock is again clearly visible and immediately behind the shock the contours are more like those in Fig. 26 due to the delay, shown in Fig. 20, before the phase effects appear. The change to the phase effect dominated neutrino evolution is responsible for the feature in the figure from $t \sim 2.5$ s, $E \sim 10$ MeV to $t \sim 4$ s, $E \sim 40$ MeV. The backwards moving reverse shock was shown in Fig. 20 to be at $E \sim 15$ MeV at $t = 6.4$ s but it is difficult to locate a feature in the positron spectrum close to this moment and energy. The late time transition in $\bar{P}_H$, shown in Fig. 21, is equally difficult to locate. Both features have been erased by the energy resolution we adopted for the detector and/or the decay of the neutrino luminosity and would require better resolution and large detector volumes in order be observable.

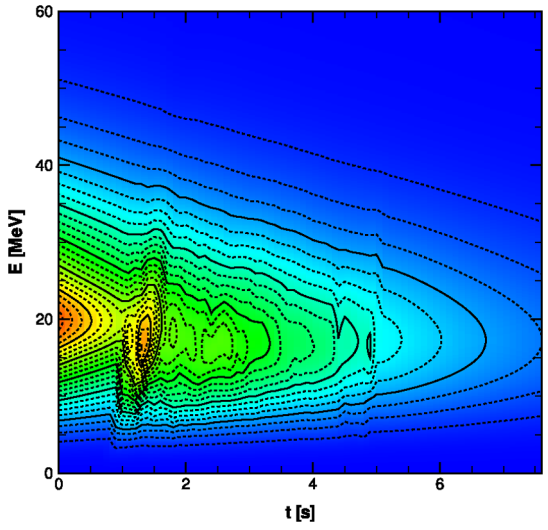

FIG. 29 (color online). The positron spectrum per unit time and per unit tonne of detector convolved with the detector resolution shown in Fig. 25 as a function of energy and time for the 1D simulation with a total energy deposition of $Q = 4.51 \times 10^{51}$ erg. Again the solid contours are evenly spaced by 10^{-3}/MeV/s/t.

VI. SUMMARY AND CONCLUSIONS

We have simulated the explosion of a $13.2M_\odot$ star in both 1D and 2D to study the effects of the evolving density profile upon the neutrinos. The explosion was achieved by depositing energy, Q, in a fashion meant to mimic neutrino heating. The energy deposition of the 1D models ranged from $Q = 1.66 \times 10^{51}$ erg up to $Q = 4.51 \times 10^{51}$ erg while for the 2D model computational limitations allowed us to only construct a single case with $Q = 3 \times 10^{51}$ erg. For the 2D model energy was deposited aspherically so that the explosion was also aspherical. From the hydrodynamical simulations we identified several prominent features—the forward shock, the reverse shock, and the density fluctuations of the 2D model—in the profiles and studied their behavior over time. We then computed the crossing probability for the matter states as they passed through the SN and showed snapshots of P_H as functions of energy. We found that the forward shock produced an easily identifiable signature in P_H but that the reverse shock and asphericity led to phase effects that made identification more tricky. We then computed the neutrino flux

at Earth and the positron spectrum one would observe in a water Cerenkov detector. Both the smearing effects—the energy distribution of the positrons for a given neutrino energy, and the energy resolution of the detector—were included. We found that the forward shock should be easily detected even with present detector technology as a feature sweeping up through the positron spectrum. Once identified, and if the progenitor were known, the information can be used to measure the shock speed, the strength of the shock, and potentially also the stalled shock time delay. Detection of the reverse shock will be more difficult while it is moving outwards but, if the reverse shock stalls and heads back to the core, then it may be spotted in the positron spectrum as a feature moving down through the spectrum. The density fluctuations upon the profile due to asphericity may not yet be detectable.

ACKNOWLEDGMENTS

The authors are very grateful to John Blondin for all his assistance with the hydrodynamic simulations and to Huaiyu Duan and Yong Qian for all their help and advice with regard to neutrino self-interactions. This work was supported by the U.S. Department of Energy at UMN under Grant No. DE-FG02-87ER40328 and at NCSU under Grant No. DE-FG02-02ER41216.

[1] S. S. Gershtein, *et al.* Zh. Eksp. Teor. Fiz. **69**, 1473 (1975).
[2] F. S. Kitaura, H.-T. Janka, and W. Hillebrandt, Astron. Astrophys. **450**, 345 (2006).
[3] L. Dessart, A. Burrows, C. D. Ott, E. Livne, S.-C. Yoon, and N. Langer, Astrophys. J. **644**, 1063 2006.
[4] J. F. Beacom, R. N. Boyd, and A. Mezzacappa, Phys. Rev. D **63**, 073011 (2001).
[5] G. C. McLaughlin and R. Surman, Phys. Rev. D **75**, 023005 (2007).
[6] D. H. Hartmann, R. D. Hoffman, S. E. Woosley, and W. C. Haxton, Nucl. Phys. **A527**, 663 (1991).
[7] A. Heger, E. Kolbe, W. C. Haxton, K. Langanke, G. Martinez-Pinedo, and S. E. Woosley, Phys. Lett. B **606**, 258 (2005).
[8] S. E. Woosley, J. R. Wilson, G. J. Mathews, R. D. Hoffman, and B. S. Meyer, Astrophys. J. **433**, 229 (1994).
[9] R. Surman, G. C. McLaughlin, and W. R. Hix, Astrophys. J. **643**, 1057 (2006).
[10] J. Pruet, R. Surman, and G. C. McLaughlin, Astrophys. J. **602**, L101 (2004).
[11] G. C. McLaughlin, G. M. Fuller, and J. R. Wilson, Astrophys. J. **472**, 440 (1996).
[12] G. C. McLaughlin and G. M. Fuller, Astrophys. J. **464**, L143 (1996).
[13] B. S. Meyer, G. C. McLaughlin, and G. M. Fuller, Phys. Rev. C **58**, 3696 (1998).
[14] T. Yoshida, T. Kajino, H. Yokomakura, K. Kimura, A. Takamura, and D. H. Hartmann, Astrophys. J. **649**, 319 (2006).
[15] G. M. Fuller, W. C. Haxton, and G. C. McLaughlin, Phys. Rev. D **59**, 085005 (1999).
[16] A. S. Dighe and A. Y. Smirnov, Phys. Rev. D **62**, 033007 (2000).
[17] J. Engel, G. C. McLaughlin, and C. Volpe, Phys. Rev. D **67**, 013005 (2003).
[18] C. Lunardini and A. Y. Smirnov, J. Cosmol. Astropart. Phys. 06 (2003) 009.
[19] A. Friedland and C. Lunardini, Phys. Rev. D **68**, 013007 (2003).
[20] R. F. Sawyer, Phys. Rev. D **72**, 045003 (2005).
[21] H. Duan, G. M. Fuller, and Y.-Z. Qian, Phys. Rev. D **74**, 123004 (2006).
[22] H. Duan, G. M. Fuller, J. Carlson, and Y.-Z. Qian, Phys. Rev. D **74**, 105014 (2006).
[23] H. Duan, G. M. Fuller, J. Carlson, and Y. Z. Qian, Phys. Rev. Lett. **97**, 241101 (2006).
[24] H. Duan, G. M. Fuller, J. Carlson, and Y.-Z. Qian, Phys. Rev. D **75**, 125005 (2007).
[25] S. Hannestad, G. G. Raffelt, G. Sigl, and Y. Y. Y. Wong, Phys. Rev. D **74**, 105010 (2006).
[26] G. G. Raffelt and A. Y. Smirnov, Phys. Rev. D **76**, 081301 (2007).
[27] J. P. Kneller and G. C. McLaughlin, Phys. Rev. D **73**, 056003 (2006).
[28] B. Dasgupta and A. Dighe, Phys. Rev. D **75**, 093002 (2007).
[29] J. M. Blondin, A. Mezzacappa, and C. DeMarino, Astrophys. J. **584**, 971 (2003).
[30] J. M. Blondin and A. Mezzacappa, Astrophys. J. **642**, 401 (2006).
[31] N. Ohnishi, K. Kotake, and S. Yamada, Astrophys. J. **641**, 1018 (2006).
[32] L. Scheck, K. Kifonidis, H.-T. Janka, and E. Muller, Astron. Astrophys. **457**, 963 (2006).
[33] A. Burrows, E. Livne, L. Dessart, C. D. Ott, and J. Murphy, Astrophys. J. **655**, 416 (2007).
[34] R. C. Schirato and G. M. Fuller, arXiv:astro-ph/0205390.
[35] K. Takahashi, K. Sato, H. E. Dalhed, and J. R. Wilson, Astropart. Phys. **20**, 189 (2003).
[36] G. L. Fogli, E. Lisi, and A. Mirizzi, and D. Montanino, Phys. Rev. D **68**, 033005 (2003).
[37] R. Tomàs, M. Kachelrieß, G. Raffelt, A. Dighe, H.-T. Janka, and L. Scheck, J. Cosmol. Astropart. Phys. 9 (2004) 15.
[38] http://wonka.physics.ncsu.edu/pub/VH-1/.
[39] P. Colella and P. Woodward, J. Comput. Phys. **54**, 174 (1984).
[40] http://www.ucolick.org/alex/stellarevolution/data.shtml.
[41] Keith Heywood (private communication).
[42] S. Choubey, N. P. Harries, and G. G. Ross, Phys. Rev. D **74**, 053010 (2006).
[43] A. Arcones, H.-T. Janka, and L. Scheck, Astron.

Astrophys. **467**, 1227 (2007).
[44] S. Samuel, Phys. Rev. D **48**, 1462 (1993).
[45] S. Pastor, G. Raffelt, and D. V. Semikoz, Phys. Rev. D **65**, 053011 (2002).
[46] M. T. Keil, G. G. Raffelt, and H.-T. Janka, Astrophys. J. **590**, 971 (2003).
[47] Y.-Z. Qian (private communication).
[48] A. B. Balantekin and J. F. Beacom, Phys. Rev. D **54**, 6323 (1996).
[49] A. N. Ioannisian and A. Yu. Smirnov, Phys. Rev. Lett. **93**, 241801 (2004).
[50] A. N. Ioannisian *et al.*, Phys. Rev. D **71**, 033006 (2005).
[51] E. Kh. Akhmedov, M. Maltoni, and A. Yu. Smirnov, Phys. Rev. Lett. **95**, 211801 (2005).
[52] C. Bemporad, G. Gratta, and P. Vogel, Rev. Mod. Phys. **74**, 297 (2002).
[53] F. N. Loreti, Y. Z. Qian, G. M. Fuller, and A. B. Balantekin, Phys. Rev. D **52**, 6664 (1995).
[54] G. Fogli, E. Lisi, A. Mirizzi, and D. Montanino, J. Cosmol. Astropart. Phys. 6 (2006) 12.
[55] A. Friedland and A. Gruzinov, arXiv:astro-ph/0607244.
[56] S. Choubey, N. P. Harries, and G. G. Ross, Phys. Rev. D **76**, 073013 (2007).
[57] R. M. Bionta, G. Blewitt, C. B. Bratton, D. Caspere, and A. Ciocio, Phys. Rev. Lett. **58**, 1494 (1987).
[58] K. Hirata, T. Kajita, M. Koshiba, M. Nakahata, and Y. Oyama, Phys. Rev. Lett. **58**, 1490 (1987).
[59] E. Kolbe and K. Langanke, Phys. Rev. C **63**, 025802 (2001).
[60] W. C. Haxton, Phys. Rev. D **36**, 2283 (1987).
[61] A. Strumia and F. Vissani, Phys. Lett. B **564**, 42 (2003).
[62] J. Hosaka *et al.* (Super-Kamkiokande Collaboration), Phys. Rev. D **73**, 112001 (2006).